LBL-32722
UC-413
Preprint

Lawrence Berkeley Laboratory
UNIVERSITY OF CALIFORNIA

Submitted to Nuclear Physics A

BUU Dynamics of Unbound Spherical Nuclei

G. Batko and J. Randrup

September 1992

REFERENCE COPY
Does Not
Circulate
Bldg. 50 Library.
LBL-32722
Copy 1

Prepared for the U.S. Department of Energy under Contract Number DE-AC03-76SF00098

DISCLAIMER

This document was prepared as an account of work sponsored by the United States Government. While this document is believed to contain correct information, neither the United States Government nor any agency thereof, nor the Regents of the University of California, nor any of their employees, makes any warranty, express or implied, or assumes any legal responsibility for the accuracy, completeness, or usefulness of any information, apparatus, product, or process disclosed, or represents that its use would not infringe privately owned rights. Reference herein to any specific commercial product, process, or service by its trade name, trademark, manufacturer, or otherwise, does not necessarily constitute or imply its endorsement, recommendation, or favoring by the United States Government or any agency thereof, or the Regents of the University of California. The views and opinions of authors expressed herein do not necessarily state or reflect those of the United States Government or any agency thereof or the Regents of the University of California.

Nuclear Physics A LBL-32722

BUU dynamics of unbound spherical nuclei *

Gustavo Batko[1] *and Jørgen Randrup*[1,2]

[1] Nuclear Science Division, Lawrence Berkeley Laboratory
University of California, Berkeley, California 94720, USA

[2] Gesellschaft für Schwerioneneforschung mbH
D-6100 Darmstadt 11, Germany

September 23, 1992

ABSTRACT:

Within the nuclear Boltzmann-Ühling-Uhlenbeck model, we investigate the dynamical evolution of spherical calcium and gold nuclei that have been agitated into unbound configurations by either compression or heating. Using a modified pseudo-particle method that preserves the spherical symmetry, we find that the conversion of the compressional energy into radial motion is only weakly dissipative and, remarkably, for a range of initial compressions between density doubling and tripling the nucleus expands to a quasi-stationary unstable bubble-like configuration. The same processes are also studied with the standard method of solution in which perfect symmetry is absent and it is shown that while the bubbles then clusterize into bound fragments, the qualitative character of the outcome is different and sensitive to the employed number of pseudo-particles per nucleon, a purely numerical parameter. Our studies suggest that for suitable initial compressions there exists a specific nuclear multifragmentation process in which the decompression leads to an unstable hollow configuration that subsequently clusterizes into massive fragments.

*This work was supported by the Director, Office of Energy Research, Office of High Energy and Nuclear Physics, Nuclear Physics Division of the U.S. Department of Energy under Contract No. DE-AC03-76SF00098.

Contents

1 Introduction **1**

2 The model **2**
2.1 Initialization 4
2.2 Spherical symmetry 5

3 Results and discussion **7**
3.1 Spherical nuclei 8
3.1.1 Effect of the Coulomb force 10
3.2 Symmetry breaking 10
3.2.1 Angular pattern 12
3.2.2 Multipolarity coefficients 13
3.2.3 Dependence on the number of pseudo-particles 15
3.3 Nuclear multifragmentation dynamics 17

4 Concluding remarks **17**

1 Introduction

In recent years, extensive experimental efforts have been devoted to the collection and analysis of multifragment data in heavy-ion collisions at intermediate energies. A major goal is to probe the properties of nuclear matter at high density and temperature. However, the degree to which this can be attained depends on our ability to model the reaction dynamics adequately. Motivated by these efforts, we have considered the dynamical evolution of highly excited spherical nuclei within the general framework of the nuclear Boltzmann-Ühling-Uhlenbeck model, the presently best founded and most successful microscopic model of nuclear dynamics at medium energies [1].

The *BUU* model propagates the reduced one-body phase-space distribution $f(\boldsymbol{r},\boldsymbol{p})$ in the self-consistent effective one-body field, while allowing the individual nucleons to experience two-body collisions subject to Pauli blocking. Our primary aims are to clarify how a highly agitated spherical nucleus actually develops according to the *BUU* model and to illustrate how the qualitative character of the outcome depends sensitively on the specific numerical method employed, a clearly unsatisfactory state of affairs. We are especially interested in starting from a compressed nucleus, since one of the main goals in the field is to learn about high-density matter, and investigate to which extent there are observable traces left over from the particular manner in which the system was initialized. This question is of obvious importance for our ability to use multifragmentation data to learn about matter under extreme conditions of compression or temperature.

A number of other studies, with differing aims, have been made by a variety of groups concerning the dynamical evolution and disassembly of excited nuclei. For example, De Paula *et al.* [2] used molecular dynamics to study the evolution of ^{197}Au after it had been excited by either compression, heating, rotation, or drilling; their results show that, for a given degree of excitation, compression is the most effective means of producing multifragmentation. As another example, several years ago Nemeth *et al.* [3] used fluid dynamics to study the evolution of hot and compressed spherical nuclei and also found that the compression is the most effective in causing breakup. They emphasized that the fluid-dynamical assumption of a vanishing mean free path is extreme and urged that complementary calculations be done with Hartree-Fock-like models (which have infinite mean free path), because the physical scenario lies in between these two extremes.

Such studies were made by Vinet *et al.* [4] with both the collisionless Vlasov model and with the *BUU* model that incorporates the average effect of the collisions. In these calculations no special effort was made to preserve the initial spherical symmetry and so the expansion into the unstable regime would always lead to the formation of fragments. Although this is also expected to happen in reality, the time scale and detailed development of the calculated fragment formation is sensitive to the value of the numerical parameter $\mathcal{N}$, the number of pseudo-particles per nucleon, and thus unreliable.

We also perform our studies within the framework of the nuclear *BUU* model, which is the appropriate model for this intermediate physical scenario. In particular, it includes the Fermi motion of the nucleons (absent in molecular dynamics) and

their finite mean free path (absent in fluid dynamics). The *BUU* model yields a mean-trajectory description and as such it preserves the initial spherical symmetry of the system. However, in most existing numerical implementations exact sphericity cannot be achieved or maintained because of irregularities associated with the adopted method of solution. When instabilities occur this feature can be a serious drawback, as we shall illustrate explicitly. We have therefore developed a modified method of solution that preserves the initial spherical symmetry and thus provides a more reliable approximation to the true solution when the dynamics is unstable.[1]

As it turns out, under suitable conditions the nucleus will expand into a hollow configuration that evolves so slowly that the instabilities have time to develop. We illustrate this important feature by the employing also the standard method of solution in which no measures are taken to avoid catastrophic symmetry breakings. The fact that such calculations are physically ill-based (because the fluctuations are of purely numerical origin) serves to emphasize the need for extending the *BUU* model to incorporate correctly the dynamical fluctuations.

The issues under consideration in the present study have gained further actuality by a number of recent *BUU* studies of nuclear multifragmentation dynamics: Moretto *et al.* [5] recently reported that the head-on collision of two Mo nuclei at typically 60 MeV per nucleon would lead to relatively thin oblate disks (so thin that the nuclear force can reach through width of the disk) which would then cluster as a result of Rayleigh-type instabilities. This remarkable result was soon followed by similar studies by other groups who found conflicting results. First, Gross *et al.* [6] considered the central collision of two Nb nuclei at 55 MeV per nucleon and found that the condensation into fragments occurs throughout the entire spherical volume, once the system has expanded sufficiently. Subsequently, Bauer *et al.* [7] considered Nb+Nb at 60 MeV per nucleon and observed the development of a transient bubble-like configuration that subsequently converts into a ring-like structure, before breaking up into fragments; they suggested that an observable consequence of this specific multifragmentation process may be an enhanced production of intermediate-mass fragments exhibiting a reduced Coulomb barrier. There is thus at the moment significant qualitative divergence with regard to understanding how the multifragmentation processes actually develop. Our present study, which is carried out for a more idealized scenario and thus is easier to analyze and discuss, may help to provide useful insight into the relevant physics.

2 The model

In the nuclear Boltzmann-Ühling-Uhlenbeck model, the temporal evolution of the one-particle phase-space density distribution, $f(\boldsymbol{r},\boldsymbol{p};t)$, is governed by the following

[1] Of course, because of the presence of instabilities, the actual physical system will exhibit a spontaneously symmetry breaking and a subsequent catastrophic divergence, and so the mean-trajectory *BUU* solution is of little practical utility.

transport equation [1],

$$\left\{\frac{\partial}{\partial t}+\frac{\boldsymbol{p}}{m}\cdot\boldsymbol{\nabla}_r-\boldsymbol{\nabla}_r U(\boldsymbol{r};t)\cdot\boldsymbol{\nabla}_p\right\}f(\boldsymbol{r},\boldsymbol{p};t)=\bar{I}[f]\ . \tag{1}$$

The left-hand side is the Vlasov part representing the collisionless propagation of the distribution in the self-consistent effective field $U(\boldsymbol{r},t)$, while the right-hand side represents the average effect of the two-body collisions,

$$\bar{I}[f_1]=\frac{1}{(2\pi)^3}\int d\boldsymbol{p}_2 d\Omega'_{12}\, v_{12}\frac{d\sigma_{12}}{d\Omega'_{12}}\left(\bar{f}_1\bar{f}_2 f'_1 f'_2-f_1 f_2\bar{f}'_1\bar{f}'_2\right)\ , \tag{2}$$

where $f_i\equiv f(\boldsymbol{r},\boldsymbol{p}_i;t)$, and $\bar{f}\equiv 1-f$ denotes the blocking factor expressing the availability of a phase-space cell near the specified phase-space location.

A variety of different methods exist for solving the *BUU* equation (1). We shall employ the method of parallel systems, in which the phase-space distribution $f(\boldsymbol{r},\boldsymbol{p},t)$ is generated by averaging over $\mathcal{N}$ systems of A pseudo-nucleons, all evolving in the same field $U(\boldsymbol{r},t)$. Thus the phase-space distribution associated with one of the parallel systems, n, is formally represented as

$$f^{(n)}(\boldsymbol{r},\boldsymbol{p};t)=h^3\sum_{i=1}^{A}\delta(\boldsymbol{r}-\boldsymbol{r}_i^{(n)}(t))\ \delta(\boldsymbol{p}-\boldsymbol{p}_i^{(n)}(t))\ . \tag{3}$$

The phase-space density distribution $f(\boldsymbol{r},\boldsymbol{p},t)$ entering in (1) is then obtained as the average of $f^{(n)}$ over the $\mathcal{N}$ parallel systems,

$$f(\boldsymbol{r},\boldsymbol{p};t)=\frac{1}{\mathcal{N}}\sum_n f^{(n)}(\boldsymbol{r},\boldsymbol{p};t). \tag{4}$$

This distribution is a solution of the homogeneous *BUU* equation (the Vlasov equation) provided that the pseudo-particles satisfy the corresponding Hamiltonian equations of motion [8],

$$\frac{d\boldsymbol{p}_i^{(n)}}{dt}=-\boldsymbol{\nabla}_r U(\boldsymbol{r}_i^{(n)},t)\ ,\quad \frac{d\boldsymbol{r}_i^{(n)}}{dt}=\frac{\boldsymbol{p}_i^{(n)}}{m_i}\ . \tag{5}$$

This system of $\mathcal{N}A$ coupled non-linear equations of motion can be integrated by employing a suitable time step δt.

The collision integral, eq. (2), is simulated numerically by allowing the pseudo-nucleons within a given system to collide with each other. When a collision happens the momenta of the pseudo-nucleons change from $\boldsymbol{p}_1$ and $\boldsymbol{p}_2$ to $\boldsymbol{p}'_1$ and $\boldsymbol{p}'_2$. The probability for the occurrence of a given collision is determined by the differential cross section $d\sigma_{12}/d\Omega'_{12}$, and by the availability of the phase-space through the blocking factors $\bar{f}$. Specific details about the simulation of the collision integral can be found in refs. [1, 9].

The essential physical input is contained in the effective field, $U(\boldsymbol{r},t)$, and in the differential cross section, $d\sigma/d\Omega$. Although both quantities can be consistently derived

within the framework of time-dependent G-matrix theory [10], for practical purposes it is necessary to express them in terms of some convenient parametrizations. Here, we adopt the parametrization proposed in [9] given by

$$U(\boldsymbol{r}) = \frac{3}{4}t_0\rho(\boldsymbol{r}) + \frac{7}{8}t_3\rho(\boldsymbol{r})^{4/3} + V_0\int d\boldsymbol{r}'\,\frac{\exp(-\mu|\boldsymbol{r}-\boldsymbol{r}'|)}{\mu|\boldsymbol{r}-\boldsymbol{r}'|}\rho(\boldsymbol{r}') + V_{\rm coul}\ , \quad (6)$$

$$\frac{d\sigma}{d\Omega}(q) = \left[\frac{mV_0}{\mu(q^2+\mu^2)}\right]^2\ , \quad (7)$$

where $q = (p-p')\sin\theta/2$ denotes the momentum transfer in the collision. The values of the parameters are $t_0 = -1124$ MeV fm^3, $t_3 = 2037$ MeV fm^4, $V_0 = -378$ MeV and $\mu = 2.175$ fm^{-1} which, for infinite nuclear matter, gives saturation at $\rho = 0.17$ fm^{-3}, a binding energy per nucleon of 16 MeV, and a nuclear compressibility modulus of $K = 238$ MeV. The known dependence of the nucleon-nucleon interactions on the momentum is sometimes taken into account in non-relativistic transport theories by adding an extra term to the mean field. However, in the present study we will neglect momentum-dependent forces and consider the effective field $U(\boldsymbol{r})$ as a functional of the spatial density $\rho(\boldsymbol{r})$ only.

2.1 Initialization

Ordinarily, when studying heavy-ion collisions, the initial positions and momenta of the pseudo-particles are picked so as to reproduce, approximately, a nucleus in its ground state (boosted appropriately). In coordinate space, this is realized by assigning to each pseudo-particle i a random position $\boldsymbol{r}_i$ picked from a specified Saxon-Woods density distribution. A good reproduction of the binding energies as well as the spatial and momentum distributions for nuclei with $A > 12$ is obtained by using $R_0 = 1.124A^{1/3}$ fm for the radius and $a = 0.024A^{1/3} + 0.29$ for the surface diffuseness [9]. The momenta are subsequently sampled from a uniform spherical distribution of radius $P_F(\boldsymbol{r}_i)$, the local Fermi momentum calculated on the basis of the Thomas-Fermi approximation.

However, for the present study we wish to start the simulation from a phase-space density distribution different from the one corresponding to the ground state. Typically, we wish to start from a compressed cold nucleus. Such a configuration can readily be obtained from the ground state by performing the simple scale transformation,

$$\boldsymbol{r}_i \to \lambda^{-1/3}\boldsymbol{r}_i\ ,\ \boldsymbol{p}_i \to \lambda^{1/3}\boldsymbol{p}_i\ . \quad (8)$$

Thus the central density in the compressed nucleus is given by $\rho(\boldsymbol{r}=\boldsymbol{0}) = \lambda\rho_0$, where ρ_0 is the central density of the ordinary nucleus.

Alternatively we occasionally wish to start from a thermally excited system. This can be achieved by picking the momenta from a finite-temperature Fermi-Dirac distribution with the specified temperature T; the local chemical potential is determined from the density $\rho(\boldsymbol{r})$.

2.2 Spherical symmetry

The structure of the *BUU* equation (1) is such that certain symmetries will be preserved if they are initially present, such as isotropy and uniformity. In particular, when the one-body phase-space density distribution is initially invariant under rotations in coordinate space, it is straightforward to verify that only central forces occur and so the spherical symmetry is preserved throughout the dynamical evolution. The one-body phase-space density can then be written as $f(r, p_r, p_t; t)$, where $r = |\boldsymbol{r}|$ is the radial distance, $p_r = \hat{\boldsymbol{r}} \cdot \boldsymbol{p}$ is the radial momentum, and $p_t = |\hat{\boldsymbol{r}} \times \boldsymbol{p}|$ is the magnitude of the transverse momentum.

The numerical method employed to solve the *BUU* problem may be briefly described as follows: Between the times t and $t + \delta t$ the $\mathcal{N}$ systems follow independent trajectories in the $6A$-dimensional phase-space, according to the equations of motion (5); the one-body phase-space density distribution $f(\boldsymbol{r}, \boldsymbol{p}, t + \delta t)$ is then obtained by averaging over these $\mathcal{N}$ systems (see eq. (4)). In this way, after each time interval δt, the fluctuations occurring from one system to another are suppressed by taking the ensemble average. The essential feature of the method is that the average phase-space density f is used as input to evaluate the effective field $U(\boldsymbol{r})$ which in turn determines the further evolution of the pseudo-particle distributions $f^{(n)}$.

Thus, the fluctuations inherent in the pseudo-particle representation are reduced but *not* eliminated in this method. Particularly, the numerical method is unable to render distributions that are exactly spherical. This shortcoming is of little import for processes in which the dynamical trajectory is stable against symmetry breaking, and arbitrarily good accuracy can then be obtained by choosing $\mathcal{N}$ large enough. However, in certain situations the equations are unstable against symmetry breaking and in such cases the method is clearly dubious, since the degree to which the instabilities will develop depends on the numerical parameter $\mathcal{N}$ (the larger the value of $\mathcal{N}$ the longer it will take before the initial irregularities in $f(\boldsymbol{r}, \boldsymbol{p})$ will manifest themselves). We shall return to this important point in Sect. 3.2.

We should emphasize that when the fluctuations are suppressed by increasing $\mathcal{N}$, then the amplitude reached in a given time by a given density instability is also suppressed, and by the same factor[2]. This feature follows from the fact that the magnitude of a certain mode α evolves approximately according to [11]

$$\dot{\sigma}_\alpha \approx 2D_\alpha + \frac{2}{t_\alpha}\sigma_\alpha \ , \tag{9}$$

where D_α is the source term arising from the fluctuations associated with the individual collision processes, and t_α is the characteristic growth time of the mode, as obtained from the dispersion relation for the system. The dynamical evolution of small density irregularities in nuclei has also recently been studied by Papp *et al.* [12]

[2]This point has not been generally appreciated - it is often argued that any noise will be amplified, so it does not matter what $\mathcal{N}$ is, but this is somewhat misleading: when the fragmenting source is expanding, the clusterization process is effectively terminated prematurely, with observable consequences as will be shown below. Only in a static scenario, with unlimited time available, will the final fragment distribution be independent of the initial irregularities.

within a hydrodynamical model. They found that at densities about 35-40 per cent of normal even the smallest fluctuations will grow, which is consistent with the results of the present study.

For now we wish to note that it is possible to modify the standard method so that the initial spherical symmetry is preserved throughout the evolution, to an arbitrary degree of accuracy. This can be accomplished by simply performing an angular averaging of $f(\boldsymbol{r}, \boldsymbol{p}; t)$ after each time step. The effective field then remains strictly spherical, thus limiting the degree to which each individual ensemble member $f^{(n)}$ can stray away from sphericity. Since we shall employ this modified method for our present studies, we describe it in somewhat more detail below.

Given the irregular matter density $\rho(\boldsymbol{r})$ at some time t, a spherically symmetric one, $\bar{\rho}(r)$, can be obtained by averaging over the directions,

$$\bar{\rho}(r) = \frac{1}{4\pi} \int_{4\pi} \rho(\boldsymbol{r})\, d\hat{\boldsymbol{r}}. \tag{10}$$

In the actual simulations, this average is calculated by binning the pseudo-particles according to their distance to the origin, r. We have employed a bin size $\delta r = 1$ fm and performed a Gaussian smearing procedure in order to obtain a smooth density distribution. The effective field, eq. (6), is then calculated on the basis of the averaged density $\bar{\rho}(r)$. The procedure removes the deviations of the field from the spherical shape that may eventually lead to further distortions in the phase-space distribution. In addition, the Fermi momentum in the initialization of the momentum distribution is also evaluated by using $\bar{\rho}(r)$, instead of $\rho(\boldsymbol{r})$.

Since the effective field now depends only on r, the calculation of $\boldsymbol{\nabla} U$ can be done more accurately. The numerical procedure consists in calculating the radial derivative at discrete points $\bar{r}_k = (r_{k+1} - r_k)/2$, by using a simple two-point formula $dU/dr|_{\bar{r}_k} \approx (U(r_{k+1}) - U(r_k))/\delta r$. Taking advantage of the fact that we have effectively only one dimension, the magnitude of the force exerted on a pseudo-particle located at r is calculated by interpolating a spline through the points $(dU/dr)_{r=\bar{r}_k}$ which satisfies the boundary condition $(dU/dr)_{r=0} = 0$. This method considerably improves the numerical accuracy. By contrast, in the standard *BUU* simulation $\boldsymbol{\nabla} U$ is calculated in a three-dimensional rectangular grid by just applying the two-point formula on each spatial direction. The force is thereby assumed to be the same for all pseudo-particles in a given cell. This usual prescription, although simple and fast, may become a very poor approximation at those points where sudden variations of the field occur (as, for example, near the nuclear surface).

The deviations from spherical symmetry originating from the stochastic simulation of the collision integral cannot be as easily eliminated. However, it is possible to suppress them considerably by imposing spherical symmetry on the Pauli blocking factors $\bar{f}$. The formal procedure is conceptually similar to what we discussed above in connection to the density, namely, to average the blocking factors over the spatial orientations. Numerically, however, the average is more efficiently evaluated by means of a Monte-Carlo technique. Specifically, for a collision taking place at the position $\boldsymbol{r}$, the *effective* blocking factor is calculated by averaging over random orientations of $\boldsymbol{r}$. This constitutes a rather simple prescription and, in addition, does not require

much additional computing time; reasonable values for the effective blocking factors are already obtained by employing only five random directions.

3 Results and discussion

We now turn to the application of the *BUU* model to the dynamics of spherical nuclei that have been highly excited by either compression or heating. Throughout, we have considered both ^{40}Ca and ^{197}Au, as representative examples of medium- or large-sized nuclei, respectively. Our primary motivation has been to examine how a nucleus responds dynamically to an initial compression. This issue is of interest in connection with current attempts to explore nuclear matter at high density by means of energetic heavy-ion collisions, in which significant density enhancements occur.

In order to have a relatively simple scenario, we have considered the *BUU* evolution of spherical nuclei that have initially been compressed by a specified factor λ. As an alternative initialization, we have instead endowed the nuclei with a corresponding amount of thermal excitation. The temperature T is then adjusted so as to ensure that the total energy of the hot nucleus equals that of the compressed nucleus with which comparison is being made. In other words, T is determined by the relation $E(\lambda, T = 0) = E(\lambda = 1, T)$. The calculated relationship between T and the compression factor $\lambda = \rho/\rho_0$ is shown is fig. 1. It is seen that the temperature T and the compression factor λ are roughly proportional, which reflects that the excitation energy depends quadratically on both T and λ, to a first approximation. Obviously, the factor of proportionality depends on the size of the nucleus considered.

With the nuclei prepared as described above, the subsequent time evolution has been obtained by solving the *BUU* equations described in the preceeding section, using the modified method that retains approximate spherical symmetry by averaging after each time step $\delta t = 0.5$ fm/c. Typically, we have used $\mathcal{N} = 100$ parallel systems in each such simulation. This relatively small value of $\mathcal{N}$ is sufficient to achieve good numerical accuracy because of the continual angular averaging.

For the discussion of the results it is useful to consider the following quantities:

Extension. The spatial size of the system is conveniently characterized by the root-mean-square radius R given by

$$R^2 = \frac{1}{\mathcal{N}} \sum_{n=1}^{\mathcal{N}} \frac{1}{A} \sum_{i=1}^{A} \boldsymbol{r}_i^{(n)} \cdot \boldsymbol{r}_i^{(n)} \ , \tag{11}$$

where $\boldsymbol{r}_i^{(n)}$ denotes the position of the ith pseudo-nucleon in the system n.

Radial flow. The rate of expansion can be described by the radial velocity v as the average radial velocity of the pseudo-nucleons,

$$v = \frac{1}{\mathcal{N}} \sum_{n=1}^{\mathcal{N}} \frac{1}{A} \sum_{i=1}^{A} \mathbf{v}_i^{(n)} \cdot \hat{\boldsymbol{r}}_i^{(n)} \ . \tag{12}$$

In addition, it is instructive to consider the time evolution of the *central density*, in units of the normal density, ρ_c/ρ_0. This quantity is initially equal to the specified value of λ (besides the fluctuations).

3.1 Spherical nuclei

The above three quantities are displayed in figs. 2 and 3 for Ca and Au, respectively. The solid curves result from the compressed initialization, using $\lambda = 2$, 2.5, and 3. When judging the degree of agitation brought about by such compressions it is helpful to note that a density doubling increases the volume energy by 8 MeV per nucleon (using $K = 238$ MeV), enough to overcome the entire binding energy of the nuclei. The systems we consider are thus all above the disassembly threshold where it is possible to disperse the system entirely into free nucleons. However, as we shall see, such a total disintegration happens only at considerably higher excitations.

At relatively moderate initial compressions ($\lambda = 2$), corresponding to the left column, the nucleus exhibits an oscillatory motion, while slowly radiating its excess excitation away by emission of individual pseudo-particles. The oscillatory character of the motion is clearly reflected in the periodic fall and rise of the central density, as well as in the periodic behavior of the radial velocity. The anharmonic appearance of the radial velocity is a consequence of the fact that the effective force acting on this quantity changes more abruptly when the system is dense than when it is dilute. Consequently, the system spends a relatively long time in the dilute configuration while the expansion slowly turns into a recontraction, whereas the system bounces back more quickly from the compression. This feature is also discernible in the plot of the central density: the system spends more time near the minima than near the maxima. The oscillatory behavior is less evident in the *RMS* radius R, since the emitted particles produce a significant and steadily growing contribution to R. This obscuring effect could be reduced considerably by suitable subtraction, or simply by imposing an upper bound on the domain considered when calculating R (as done in fig. 15). The continual loss of energy carried off by the emitted particles appears to be the main source of the damping of the collective radial motion.

We observe that the period depends on the size of the system. Furthermore, as the initial compression is increased, the period of the oscillations grows longer and the rate of particle emission increases. At some point, the initial compression exceeds a critical value and the systems keeps expanding monotonically. This qualitative change in behavior happens for $\lambda \approx 2.5 - 3$ for Ca and for $\lambda \approx 2 - 2.5$ for Au. The central density then quickly drops to zero and, after its first maximum, the radial velocity falls steadily towards a constant value characterizing the outwards flow of the totally dispersed pseudo-particles; this value depends directly on the initial compression via energy conservation. The *RMS* size attains the same asymptotic behavior and we have $\dot{R} = v$. [We note that total disintegration into free nucleons can only take place when $E > 0$; for smaller excitations the disassembly must involve bound clusters.]

In figs. 2 and 3 we have included the result of the respective alternative scenarios when the same degree of excitation has been achieved by thermal excitation instead.[3] It is evident from the plots that the thermal initialization is much less effective in generating collective radial motion, as one might perhaps have suspected. The hot nucleus principally exhibits an evaporation-like behavior, radiating pseudo-particles

[3]In fact, these hot configurations are slightly compressed relative to the equilibrium configurations at the specified temperature, since nuclei expand as they heat up, like most physical systems.

while gradually shrinking and cooling. The question of how much mass is lost by this type of deexcitation process has been studied in ref. [2]. It should be noted, though, that in the case of the relatively large gold nucleus the thermal pressure is in fact able to produce some collective motion, especially for excitations near the critical one, as is borne out by the behavior of the central density for $T = 13.4$ MeV ($\lambda = 2.5$).

The collision rate per nucleon occurring in the simulations is remarkably small, with typical values of order 10^{-2} (fm/c)$^{-1}$. For the case of the compressed initialization, it shows a rapid increase at the beginning of the expansion (it is initially zero due to the Pauli blocking) but, as the nucleus continues expanding, it reaches a maximum and then decreases becoming negligible when the system attains its dilute stage. On the other hand, when the nucleus has been thermally agitated the collision rate stays rather constant during the entire time evolution.

A more detailed picture of the evolution is provided by the radial density profile $\rho(r,t)$, which is easy to display because of the spherical symmetry (and which can be extracted with good numerical accuracy for the same reason). In fig. 4, we display the density profile obtained for ^{40}Ca. In the cases corresponding to the thermal initialization (dashed curves) the shape of the density profile is little affected, consistent with the approximate characterization of the process as evaporation from a hot compound nucleus. By contrast, the density profile becomes drastically distorted when compressed initializations are employed. For $\lambda = 2.5$, close to the critical value, the calculations indicate that the matter moves out from the central region to form a bubble-like configuration: the central density is more dilute than its surroundings. After spending a considerable length of time in such a state, the nucleus recontracts in response to the cohesive action of the mean field and the oscillatory situation is established. However, if the initial compression is further increased the mean field is no longer able to reverse the outwards motion and the nucleus disperses into its constituents, as is shown by the results for $\lambda = 3$.

The corresponding results for ^{197}Au are shown in fig. 5. They show that the development of a bubble configuration is more pronounced for the heavier system. Furthermore, the compressed initialization leads to the formation of a bubble already for $\lambda = 2$. In contrast with the lighter system, for sufficiently high temperatures the thermal initialization also generates a bubble-like appearance of the density, although much less developed than for the corresponding compressional initialization.

We note in passing that our results are rather similar to what has been obtained with the *TDHF* model [13] (which also preserves the spherical symmetry), as might be expected because the effect of the nucleon-nucleon collisions is relatively small in the present *BUU* simulations.

In summary, when solved properly (*i.e.* preserving the initial spherical symmetry) the *BUU* model predicts that an initially compressed nucleus will rapidly expand and then, depending on the degree of the initial compression, either recontract and oscillate (subject to mass loss by particle emission) or undergo a complete disintegration into a dilute gas. Moreover, the conversion of the initial excitation energy into collective radial motion is very sensitive to the way in which that energy is stored in the system during the initialization, as evidenced by our comparisons between compression and heating.

3.1.1 Effect of the Coulomb force

It is interesting to examine the role played by the Coulomb force in the dynamics. For this purpose, we have calculated the expansion of "uncharged" ^{197}Au initially compressed at $\lambda = 2.5$, by setting to zero the last term in eq. (6). The comparison with the results obtained by using the full mean field is displayed in fig. 6 by the solid lines, while the dashed lines denote the calculated values without the Coulomb force. As expected, the uncharged nucleus is more cohesive, as is clearly manifested in the recontraction. However, it still leads to the formation of a bubble. The results suggest that the uncharged system behaves in a fashion very similar to the charged one provided it is compressed correspondingly more so as to contain the same potential energy. A simple estimate for $A = 197$ shows that the same compressional energy obtained for the uncharged system using $\lambda = 2.5$ results when compressing the charged system using the somewhat smaller value $\lambda = 2.3$. It can be readily verified that this is consistent with the results displayed in fig. 3.

Our calculations thus indicate that the Coulomb force is not a major factor in the formation of a hollow configuration nor for its longevity (it stays for about 100 fm/c also when the Coulomb force is absent). Rather, the dynamical behaviour appears to be mainly determined by the total compressional energy of the system, both nuclear and Coulomb, with only a minor dependence on temperature. In a nuclear collision the amount of compressional energy stored early on, for a given bombarding energy, depends on the degree of dissipation which in turn is a sensitive function of the nucleon-nucleon collisions. It would therefore be of interest to devise means of directly ascertaining the degree of compression achieved.

3.2 Symmetry breaking

The above results suggest that, under special initial conditions, the system approaches a situation where the cohesive pull by the mean field largely cancels the outwards motion and, as a result, the system spends a considerable time as a bubble. In this configuration the maximum density in the system is less than $0.4\rho_0$. Such conditions of density and temperature lie well within the region of mechanical instability of the nuclear phase diagram. Furthermore, the time spent under these unstable conditions might be as large as 100 fm/c, which is longer than the growth times for density nonuniformities [14]. One must therefore expect that the bubble will undergo a spontaneous transformation, leading to condensation into a number of fragments and an associated loss of spherical symmetry. The description of such a process lies outside the scope of the standard *BUU* model which addresses only the mean trajectory and therefore is inadequate for unstable evolutions.

There are currently several efforts underway to include the fluctuating part of the *BUU* collision integral into the description of nuclear dynamics, leading to the nuclear Boltzmann-Langevin model [15, 16]. However, although significant progress has already been made in this regard, no numerical implementation is yet available that is both tractable and accurate.

We have therefore undertaken to make a preliminary qualitative investigation of

the expected clusterization process. For this purpose we have considered the same dynamical problems as discussed above using the standard *BUU* treatment without any enforcement of spherical symmetry. The fact that we consider a finite number of parallel systems, $\mathcal{N}$, implies that the extracted density distribution, and associated quantities such as the effective field, will possess irregular deviations from spherical symmetry at the outset. These fluctuations may then act as seeds for the catastrophic amplification process mentioned above, and the system may undergo actual clusterization, provided that the dynamics takes it into the unstable regime.

We saw above that when spherical symmetry is enforced the critical compression (*i.e.* that initial compression for which the nuclear cohesion exactly halts the outwards motion) appears to lie in the range $2.5 < \lambda_c < 3$ for ^{40}Ca and $2 < \lambda_c < 2.5$ for ^{197}Au. We expect that a standard *BUU* calculation (*i.e.* without strict symmetry) will yield a lower value of λ_c, since the amplification of the inherent fluctuations makes the system more fragile. Therefore, we have studied the cases corresponding to the lower end of these intervals, namely $\lambda = 2.5$ for ^{40}Ca and $\lambda = 2$ for ^{197}Au.

The results are illustrated in figs. 7 and 8. For reference the symmetric results discussed above are included on the right. The other curves are extracted from five independent *BUU* runs, each using $\mathcal{N}$ parallel systems of pseudo-particles, and the shaded areas indicate the associated standard deviation. The five runs differ only in the initial random population of the phase space. Furthermore, in order to study the dependence on the magnitude of the inherent statistical fluctuations, we have made the calculations using two different values of $\mathcal{N}$ for each system.

Let us first consider the results for ^{40}Ca (fig. 7). As already discussed above, when spherical symmetry is maintained, the system first expands to a bubble and then recontracts at about $t = 100$ fm/c. When the standard *BUU* simulation is employed the results depend drastically on the value of $\mathcal{N}$. For $\mathcal{N} = 200$, which is a typical value employed in heavy-ion studies, the recontraction does not take place; instead the system responds to the dilution by binding into clusters so that the overall expansion can be continued. On the other hand, for sufficiently large values of $\mathcal{N}$ the results will follow closely the symmetric ones (up to a certain time that increases with $\mathcal{N}$). This feature is illustrated by the results for $\mathcal{N} = 800$ (for which the magnitude of the initial fluctuations are halved) which show a much closer correspondence with the symmetric ones. Nevertheless, the recontraction occurs at a significantly later time and the central density peaks at a smaller value.

In the case of ^{197}Au (fig. 8) the results obtained with the standard *BUU* simulation are significantly different from those obtained by enforcing the spherical symmetry: for the two cases shown ($\mathcal{N} = 100$ and 300) there is no oscillatory motion. It is important to note that even though the dynamical evolutions of the various quantities that characterize the radial motion differ from the corresponding spherical situation, the results obtained in the five independent runs are rather similar to one another, as reflected in the relatively small standard deviation. This feature suggests that, for a given value of $\mathcal{N}$, the overall evolution is rather independent of the particular noise pattern in the initial density (although of course, the detailed evolutions differ markedly from case to case with respect to the sizes and locations of the clusters that are formed). As the above results illustrate, it must be expected that the number of

parallel systems needed to achieve a reasonable degree of accuracy in the simulation depends crucially on the time spent in the unstable regime.

The qualitative difference between the symmetric evolution and the irregular ones is well illustrated in figs. 9 and 10 which display the time evolution of the density profile. For the standard *BUU* calculations the effective density profiles $\tilde{\rho}(r)$ have been obtained by averaging each actual irregular density $\rho(\boldsymbol{r})$ over the direction $\hat{\boldsymbol{r}}$ (see eq. (10)); the error bars indicate the standard deviation obtained with the five independent runs. The solid line shows the symmetric result.

The result for ^{40}Ca (fig. 9) shows approximately the same density profile and small fluctuations up to about 60 fm/c. At that time, the system reaches its most dilute configuration, with densities of about $0.15-0.20\rho_0$. From there on, the radial profile of the density distribution obtained with the standard simulation deviates qualitatively from the one that corresponds to the spherically symmetric case, and the fluctuations grow larger.

For the heavier nucleus ^{197}Au (fig. 10) the differences between the symmetric and the standard simulation appear at earlier times. Both density profiles show a bubble-like configuration. As we shall see below, in the irregular case the actual density distribution is clustered. As a consequence, the restoring force acting of R is considerably smaller and the matter is situated farther out (and is somewhat more dispersed radially). Remarkably, the system remains almost stationary for times up to at least 100 fm/c.

In summary, at the early stage the standard simulation method yields dynamical evolutions that agree well with those for which the initial symmetry has been enforced. However, once that the system reaches the dilute unstable configuration, the results obtained with the standard *BUU* method deviate qualitatively from the symmetric ones. We emphasize that the symmetry breaking is merely the result of numerical noise due to the finite value of $\mathcal{N}$. Those irregularities induce the system to follow divergent dynamical trajectories, all of which differ qualitatively from the proper solution of the *BUU* equation.

3.2.1 Angular pattern

The above analysis was based on dynamical quantities that have been averaged over the spatial direction. However, our particular example indicates that the initial deviations from spherical symmetry give rise to fluctuations in the effective field that are subsequently amplified affecting the further evolution. More insight into this key phenomenon can be gained by studying the angular distribution of the matter.

A very direct illustration of the clusterization taking place is given in fig. 11 which shows a contour map of the density distribution projected onto the unit sphere,

$$\tilde{\rho}(\hat{\boldsymbol{r}}, t) = \frac{4\pi}{A} \int dr\ r^2 \rho(\boldsymbol{r}, t)\ . \tag{13}$$

Such a display is similar to a map of the world, with the azimuthal angle ϕ playing the role of the longitude and the polar angle θ replacing the latitude.

The growth of instabilities in the standard *BUU* simulation is immediately appreciated from the results shown in fig. 11. The figure displays the time evolution

the projected density distribution $\tilde{\rho}(\hat{\boldsymbol{r}}, t)$, for ^{197}Au initially compressed to double density ($\lambda = 2$), as a function of the polar angle θ and the azimuthal angle ϕ. The density profile discussed in the preceeding section shows that the system develops into a configuration where the matter is confined within a rather well-delineated shell (a bubble). Therefore it is reasonable to make the radial projection (13). The result shown corresponds to one particular simulation, employing $\mathcal{N} = 300$ parallel systems. The radial projection is normalized so that it is unity for a distribution having spherical symmetry, thus facilitating the recognition of irregularities. The contour levels corresponding to that value are indicated by the dashed line, while the solid lines indicate the contours associated with densities that are 2, 3, and 4 times larger.

As expected, early on the system displays an approximately isotropic angular pattern, exhibiting only small statistical fluctuations. Between 75 and 90 fm/c some regions having twice the initial density appear. A comparison with the time evolution of the corresponding radial distributions shown in fig. 10 reveals that the system has already spent about 40 fm/c in a situation where its density is less that $0.3\rho_0$. As time progresses, the irregularities continue to develop and the system exhibits a more defined angular structure. At 150 fm/c, it displays a clear clusterization pattern. We wish to emphasize that the dynamical processes has not yet been completed at 150 fm/c and therefore the system may undergo further changes in its structure. We return to this important point later in this section.

3.2.2 Multipolarity coefficients

The displays in fig. 10 has an obvious intuitive appeal and shows qualitatively how the instabilities grow in the system. A more quantitative description is made below.

We have seen that the excited nucleus tends to expand into a fairly hollow matter distribution, after which the inherent instabilities begin to manifest themselves as the density undergoes a rapid clusterization. The macroscopic characteristics of this process can be conveniently described by the following multipole coefficients,

$$\alpha_{lm} = \int \frac{d\boldsymbol{r}}{A}\, \rho(\boldsymbol{r})\, Y_{lm}(\hat{\boldsymbol{r}}) = \frac{1}{\mathcal{N}} \sum_{n=1}^{\mathcal{N}} \frac{1}{A} \sum_{i=1}^{A} Y_{lm}(\hat{\boldsymbol{r}}_i^{(n)}) \ , \tag{14}$$

where Y_{lm} is the usual spherical harmonic. In the last relation we have used the representation (10) of the density distribution in terms of the positions of the individual pseudo-particles, $\boldsymbol{r}_i^{(n)}$. The utility of the coefficients α_{lm} is enhanced by the fact that the distribution considered has a hollow appearance, so that the matter is concentrated in a relatively thin shell. For more general profiles, a suitable modulation of the radial distribution may be required.

Since there is no preferred direction for the scenarios considered here, it is natural to define the quantity

$$a_l = \frac{4\pi}{2l+1} \sum_{m=-l}^{l} |\alpha_{lm}|^2 = \frac{1}{\mathcal{N}^2} \sum_{nn'}^{\mathcal{N}} \frac{1}{A^2} \sum_{ij}^{A} P_l(\cos\theta_{ij}^{(nn')}) \ . \tag{15}$$

This directional average is conveniently normalized so that a_0 is unity. The second relation exploits the representation of the Legendre polynomial P_l in terms of spherical harmonics, and the double sum over pseudo-particles includes the diagonal term having $n' = n$ and $i = j$. The argument in the Legendre polynomial is determined from the relation $\boldsymbol{r}_i^{(n)} \cdot \boldsymbol{r}_j^{(n')} = r_i^{(n)} r_j^{(n')} \cos\theta_{ij}^{(nn')}$.

In fig. 12 we show the values of the pattern coefficients a_l as extracted from a sample of five dynamical evolutions for the ^{197}Au initially compressed at $\lambda = 2$ (and using $\mathcal{N} = 300$). At the beginning, the coefficients corresponding to $l > 0$ vanish, consistent with a spherical distribution. At about $t = 70$ fm/c, the effect of the symmetry breaking becomes noticeable in the growth of the pattern coefficients. At that time the system has already become dilute (see fig. 10) and the instabilities are able to develop (see fig. 11). From there on, the results further deviate from the spherical shape. The coefficients corresponding to l =3, 4 and 5 attain the largest values. However, in contrast to the quantities associated to the radial motion (see fig. 8) they fluctuate more from one run to the other, as is evident from the indicated standard deviation.

There are several advantages to considering the multipole coefficients in the discussion of multifragmentation processes. Firstly, the coefficients α_{lm} provide a general and systematic description of the angular pattern. Secondly, the multipole coefficients can be readily extracted from microscopic transport models, even when these models do not yield a good description of the actual cluster formation, since only the matter density $\rho(\boldsymbol{r})$ is required. [For example, in fluid dynamics only the structureless matter distribution in known, and the same is true in the *BUU* model, while molecular dynamics yields the positions of the individual nucleons but is unable to reliably predict how these will ultimately cluster.]

Thirdly, the quantities a_l can relatively easily be extracted from data on multifragment events, provided that the kinematical coverage is reasonably complete. It may therefore constitute a powerful tool in the comparison of data with theoretical predictions, avoiding the tedious task of determining the cluster structure of the matter distribution.

It would appear that this kind of multifragment analysis is particularly suited for emulsion data, since these have essentially complete dynamical coverage (for charged fragments) and, moreover, the relative paucity of analyzed events (typically only of the order of several hundreds), which is the inherent weakness of emulsion data, should be no serious problem in the present context, since such event numbers should suffice to achieve useful determinations of the pattern coefficients a_l (recall that the results in fig. 12 have been obtained on the basis of only five events). We therefore suggest that such analysis be made for existing emulsion data. By utilizing the above expression (15) it would be quite straightforward to calculate the values of a_l event by event. It should be emphasized that it would probably be important to consider only the most central events, to avoid mixing of different flow patterns. This can probably easily be achieved by focussing on the most fragment-rich events (these are anyway those to which most analysis effort has been devoted). The multipole coefficients α_{lm}

defined in eq. (14) can be extracted from a given multifragment event as

$$\alpha_{lm} = \frac{1}{A}\sum_{n=1}^{N} A_n Y_{lm}(\hat{\boldsymbol{p}}_n) \approx \frac{1}{Z}\sum_{n=1}^{N} Z_n Y_{lm}(\hat{\boldsymbol{p}}_n) \ . \tag{16}$$

Here the N observed fragments have the momenta $\{\boldsymbol{p}_n\}$ and the mass numbers $\{A_n\}$, with $A = \sum_n A_n$. Often only the fragment charge Z_n is measured and should then be used in place of the mass number A_n, as indicated in the last expression above. This lack of completeness in the data should not introduce significant distortions of the extracted coefficients, because the global angular distributions of neutrons and protons tend to be similar.

We wish to stress that the present study considers the evolution of sources that have been carefully prepared to have spherical symmetry. This initialization is convenient for our present purposes. However, in a collision experiment there is hardly spherical symmetry at any point during the evolution. Instead, there is approximate axial symmetry, for sufficiently central events. Therefore the above directional average leading to a_l should be modified and one should instead consider the pattern coefficients $a_{lm} = \frac{1}{2}(|\alpha_{lm}|^2 + |\alpha_{l-m}|^2)$.

3.2.3 Dependence on the number of pseudo-particles

We saw in Sect. 3.2 that the evolution of the collective flow and the radial distribution of the system is strongly dependent on $\mathcal{N}$, the number of pseudo-particles per nucleon used in the simulation. In addition, the symmetry breaking produced by these numerical fluctuations causes significant alterations of the structure of the system when it enters into the unstable regime. Of course, the two effects are closely related since the development of the irregular structure reduces the overall cohesion of the system, thus inhibiting its ability to counteract the expansion.

The magnitude of the fluctuations producing the catastrophic changes in the structure is directly related to the numerical parameter $\mathcal{N}$. Recent simulations of actual nucleus-nucleus collisions have yielded contradictory results depending on what value of $\mathcal{N}$ was employed [5, 6, 7]. Thus, it is essential to determine the qualitative (and, if possible, also the quantitative) implications that the use of a different number of parallel systems will have on the dynamical features obtained from simulations based on transport theories.

In order to shed some light on this essential question, we have computed two single *BUU* dynamical histories up to 285 fm/c, using $\mathcal{N} = 100$ and 300, respectively. The qualitative differences are clearly brought out by the results of fig. 13, which displays the projected density distribution as a function of the polar angle θ and the azimuthal angle ϕ, in the same fashion as in fig. 11, for ^{197}Au compressed at double density ($\lambda = 2$). The simulations differ *only* in the number of parallel systems utilized, $\mathcal{N} = 100$ or 300, respectively (the run with $\mathcal{N} = 300$ has a different initial seed than the one displayed in fig. 11, thus showing how the random random initialization lead to different angular patterns). At 75 fm/c, shortly after the system has entered into the unstable regime, the simulation with $\mathcal{N} = 100$ (left) has developed significant irregularities. By contrast, when 300 pseudo-particles are used (right) the

irregularities are not yet apparent. This clearly illustrates that when the initial fluctuations are reduced (by a factor 0.58 in this particular case) the amplitude reached at a given time by a specific density instability is reduced accordingly (see eq. (9)). At 150 fm/c both systems exhibit a cluster structure. However, the irregularities that have developed in the simulation having $\mathcal{N} = 100$ are more clearly delineated and have reached larger amplitudes than those of the counterpart obtained with $\mathcal{N} = 300$. At later times the differences grow even larger and at the end of the calculation the two simulations show little resemblance with one another: the one performed with $\mathcal{N} = 100$ has produced eight separated fragments of comparable mass, whereas the irregularities that appeared in the one with $\mathcal{N} = 300$ have reunited into a single very distorted object, which will presumably develop into a compound nucleus rather than undergo multifragmentation.

In a more quantitative fashion, fig. 14 shows the time evolution of the corresponding pattern coefficients a_l, as extracted from those simulations. When the dynamics is simulated with $\mathcal{N} = 100$ the angular pattern is characterized by a mixture of multipolarities. It is noteworthy that the largest values of a_l occur for $l = 3$ and 4, which is probably related to the multiplicity of fragments. For $\mathcal{N} = 300$, the coefficients with $l = 4$ and 5 become initially dominant but they decrease considerably at later times, and at the end the angular pattern is determined by a combination of a quadrupole and a octupole deformation. This behavior is a reflection of the fact that the system is then in the process of recombining into a compound nucleus. The connection between the multipolarity and the cluster multiplicity is again manifested in the fact that a_5 begins to decrease earlier than a_4. Moreover, the results at the end of the simulation indicate that a_3 saturates (and perhaps even decreases at later times), while a_1 and a_2 show an increasing trend.

A closer inspection of the respective radial patterns may both complement and elucidate the previous discussion. Therefore, in fig. 15 we show the corresponding radial velocity as well as the radial profile of the density distribution, for the respective simulations. In this case, the radial velocity reflects the average collective flow of those particles located within a sphere of radius 20 fm, thus eliminating the flow component associated with the fastest nucleons (about 18% and 15% of the total mass for $\mathcal{N}$ = 100 and 300, respectively). The slow increase in the radial flow is due to the Coulomb repulsion. It should be noted that the radial velocity is very small for the simulation corresponding to $\mathcal{N} = 300$ once that the system enters the unstable region. Moreover, it becomes negative between 115 and 200 fm/c. This is also reflected in the radial shape of the density distribution, which shows that the system experiences a recontraction after 150 fm/c. On the contrary, when the dynamics is simulated with only $\mathcal{N}$=100 pseudo-particles the system posses and maintains a sufficient amount of outwards motion to allow multifragmentation to occur.

In summary, we have shown that depending on the number of pseudo-particles employed to simulate the dynamical evolution one may obtain radically different results under otherwise similar circumstances. By increasing the numerical parameter $\mathcal{N}$ one reduces the magnitude of the fluctuations which delays the development of the instabilities. At the same time, there is less radial motion available since the system remains more symmetric and, consequently, more cohesive.

3.3 Nuclear multifragmentation dynamics

The multifragmentation scenario can then be understood as the result of a delicate interplay between the magnitude of the fluctuations, the characteristic time for the growth of the instabilities, and the amount of radial motion of the system. Provided that the dynamical problem is correctly solved and that the initial conditions drive the system into the unstable regime, the fluctuations are responsible for the spontaneous breaking of the symmetry that allows triggering and development of the instabilities. When the radial flow is large, as it will be when the initial compression is well above the critical value, then the outwards motion will persist and there will be insufficient time for the irregularities to grow into intermediate-mass clusters; the system will then disassemble into many light fragments. On the other hand, when the radial flow is below critical the system will tend to recontract so that the prefragments that may have developed will fuse with one another and a compound-like system will result. Clearly, in order to avoid conflicting results, it is important to treat the fluctuations properly, since their character and magnitude affect the radial motion significantly and thus determine the critical compression.

As a consequence, the degree to which the outwards flow (which becomes the fragment kinetic energy) can be used to probe the initial compression in a realistic collision scenario is hampered by a strong dependence on the numerical parameter $\mathcal{N}$. However, the density compression reached in the collision is determined by the dynamics during the early stage of its evolution, when the *BUU* transport model still provides a reliable description. Therefore, if the magnitude of the initial compression can be established by such means, the observed radial flow could be exploited as a sensitive indicator of the fragmentation dynamics, particularly about the size of the fluctuations and the time scale of the clusterization process.

4 Concluding remarks

We have studied the dynamical evolution of a nucleus that has been prepared in an excited but spherically symmetric configuration, generated either by compressing the ground state by a specified factor λ or by heating its local Fermi-Dirac momentum distribution correspondingly. The systems considered all lie above the disassembly threshold and so it is energetically possible to disperse the system into its nucleon constituents. The dynamical evolutions have been calculated within the general framework of the Boltzmann-Ühling-Uhlenbeck model, using a commonly employed method of solution that propagates $\mathcal{N}$ (≈ 100) A-body systems in the same effective one-body field. We have modified an existing code so as to ensure that the initial spherical symmetry is preserved, even when the system is situated in a mechanically unstable region of the phase diagram.

The imposition of spherical symmetry initially is an idealization that is not likely to be achieved in a real collision. Nevertheless, it illustrates well the important role played by irregularities of numerical origin. The proper solution of the *BUU* equation in a collision geometry will still yield a regular (though not perfectly symmetric) distribution whose further evolution may differ qualitatively from the evolution of

the distribution endowed with numerical irregularities.

Because the standard *BUU* model describes the mean trajectory, the initial spherical symmetry is preserved throughout (if the equation is solved correctly) and so only monopole modes can occur. For moderate compressions the nucleus exhibits a weakly damped monopole oscillation, whereas for large initial compressions the radial motion induced by the release of the compressional energy is sufficient to cause the system to disperse into a dilute nucleon gas. For a range of intermediate values of the initial compression factor λ the expanded system lingers for a relatively long time in a hollow bubble-like configuration while continually radiating nucleons.

During this bubble stage the system is unstable against clusterization into fragments of more favorable density. We have illustrated this tendency towards spontaneous symmetry breaking by studying these situations with the standard *BUU* method which allows such catastrophic evolutions. Because only a finite number of parallel systems $\mathcal{N}$ are treated, this standard method is endowed with considerable inherent irregularities and thus the unstable modes may be readily triggered. This is indeed what happens and by projecting the hollow density distribution onto a sphere (which may be subsequently projected onto a planar representation) the clusterization can easily be observed visually.

As a quantitative characterization of the clusterization phenomenon, we have introduced the pattern coefficients a_l based on the standard multipole moments of the matter density distribution. On the basis of a small test sample of *BUU* histories, we have found that certain of these pattern coefficients attain appreciable values, while the others are less significant. Since the evolution of the clusterization depends on the characteristic dynamical properties of the nuclear matter, especially the dispersion relation which governs the amplification rates, this kind of information is useful as it may help constrain the parameters in our nuclear models. We are suggesting that the extraction of pattern coefficients may be an especially suitable method of analysis for emulsion data for high-multiplicity events. Of course, such an analysis may also be applied to multifragment data obtained with electronic detector arrays, provided the angular coverage is sufficiently complete.

We have seen that an initially compressed nuclear sphere tends to expand into a bubble-like configuration. Similar evolutions have been obtained earlier with both molecular dynamics [2] and fluid dynamics [12]. Moreover, the recent *BUU* calculations by Bauer *et al.* [7] indicate that an approximately spherical compressed source may actually be formed in nuclear collisions and subsequently expand to a bubble or ring configuration.[4] The appearance of a hollow spatial density distribution is thus probably a rather general feature of the explosive expansion following high compression.

Nevertheless, it appears that the formation of a hollow matter distribution has not been generally anticipated in the formulation of statistical models for multifragmentation which typically employ sources with uniform interiors [17, 18, 19]. If indeed

[4]It should be noted, though, that other *BUU* studies [5, 6] have given conflicting results. These three groups [5, 6, 7] have employed different values of the numerical parameter $\mathcal{N}$, the number of pseudo-particles per nucleon (namely, $\mathcal{N}$ = 40, 150 (or 300), and 1000, respectively) and it would be informative to compare their results for the same values of $\mathcal{N}$.

the source is hollow, these models should be modified accordingly. Both the Coulomb energy and the relation between the source radius and the effective freeze-out volume are significantly altered, and the overall radial motion should also be incorporated. (The reduction of the Coulomb barrier was already discussed by Bauer *et al.*[7].) Furthermore, it should be expected that source sizes extracted by interferometry methods can be large without the source being correspondingly dilute. Indeed, it may be predicted that Hanbury-Brown/Twiss analysis of sources leading to multifragmentation will yield relatively large sizes consistent with a hollow breakup configuration.

In general, the largest fragments ought to form at the lowest possible compression that does not turn back into a compound system. When this limit is approached the overall outwards motion is fairly small. It can be then expected that the complex fragment multiplicity increases steadily from one below critical through two, three, ... just above critical, to an ever larger number of ever lighter fragments as the compression is increased. Thus there should be a correlation between the fragment sizes of an event and the overall outwards motion (or kinetic energy).

In heavy-ion collisions at intermediate energies, where large multiplicities of massive fragments occur, the density compression hardly gets above doubling, and so the conditions for a total vaporization are not present. Therefore, the disassembly can only occur via breakup into bound fragments and thus the outcome of a dynamical calculation is expected to be delicately dependent on the treatment of the fluctuations. The present study thus serves to draw attention to the importance of developing physically sound dynamical models that include the occurrence of fluctuations. Although such efforts are already well underway [15, 16], the extended models are still too computer demanding to be of direct practical utility and there is a need for developing more tractable approximate methods.

Perhaps most importantly, our present studies suggest the existence of a specific nuclear multifragmentation process by which an initially compressed nuclear system disassembles into several massive fragments. The characteristic feature is a decompression leading to an unstable hollow structure whose global evolution is sufficiently slow to allow the instabilities to manifest themselves, resulting in a clusterization of the structure into disjoint prefragments. Although our study has been carried out for an idealized spherical geometry, recent calculations indicate that such a scenario may be approximately reached in actual central heavy-ion collisions at intermediate energies [7]. This novel process displays an intricate interplay between the time scale for the global expansion dynamics and those for the triggering and amplification of the various unstable modes. The qualitative identification and quantitative exploration of this process would provide important new experimental information on nuclear dynamics.

References

[1] G.F. Bertsch and S. Das Gupta, Phys. Rep. 160 (1988) 189.

[2] L. De Paula, J. Nemeth, Sa Ben-Hao, S. Leray, C. Ngô, H. Ngô, S.R. Souza, and Zheng Yu-Ming, Phys. Lett. B258 (1991) 251.

[3] J. Nemeth, M. Barranco, C. Ngo, and E. Thomasi, Z. Phys. A323 (1986) 419; Z. Phys. A325 (1986) 347.

[4] L. Vinet, C. Grégoire, P. Schuck, B. Rémaud, and F. Sebille, Nucl. Phys. A468 (1987) 321.

[5] L.G. Moretto, K. Tsuo, N. Colonna, G.J. Wozniak, preprint LBL-31812 (1992), subm. to Phys. Rev. Lett.

[6] D.H.E. Gross, Bao-An Li, and A.R. DeAngelis, HMI preprint (June 1992).

[7] W. Bauer, G.F. Bertsch, H. Schultz, preprint MSUCL-840 (June 1992).

[8] C.Y. Wong, Phys. Rev. C25 (1982) 1460.

[9] W. Cassing, V. Metag, U. Mosel and K. Niita, Phys. Rep. 188 (1990) 363.

[10] W. Cassing, K. Niita and S.J. Wang, Z. Phys. A331 (1988) 439.

[11] G.F. Burgio, Ph. Chomaz, J. Randrup, Phys. Rev. Lett. (1992), in press.

[12] G. Papp, J. Németh, and J.P. Bondorf, Phys. Lett. B278 (1992) 7.

[13] A. Dhar and S. Das Gupta, Phys. Rev. C30 (1984) 1545.

[14] C.J. Pethick and D.G. Ravenhall, Ann. Phys. 183 (1988) 131; H. Heiselberg, C.J. Pethick, and D.G. Ravenhall, NBI preprint (1992).

[15] S. Ayik and C. Gregoire, Phys. Lett. B212 (198) 269; Nucl. Phys. A513 (1990) 187.

[16] Ph. Chomaz, G.F. Burgio, J. Randrup, Phys. Lett. B254 (1991) 340;
G.F. Burgio, Ph. Chomaz, J. Randrup, Nucl. Phys. A529 (1992) 157.

[17] S.E. Koonin and J. Randrup, Nucl. Phys. A356 (1981) 223; *ibid.* A474 (1987) 173.

[18] D.H.E. Gross, Phys. Lett. B161 (1985) 47; D.H.E. Gross, X.Z. Zhang, and S. Y. Xu, Phys. Rev. Lett. 56 (1986) 1544.

[19] J.P. Bondorf, R. Donangelo, I.N. Mishustin, C.J. Pethick, and H. Schulz, Nucl. Phys. A443 (1985) 321; J.P. Bondorf, R. Donangelo, I.N. Mishustin, and H. Schulz, Nucl. Phys. A444 (1985) 460.

Figure 1: Heating versus compression.
For either ^{40}Ca or ^{197}Au, the plot shows that value of the nuclear temperature T which produces the same total energy E as obtained by instead compressing the cold nucleus by the factor $\lambda = \rho/\rho_0$ (so that $E(T = 0, \rho = \lambda\rho_0) = E(T, \rho)$).

Figure 2: Collective flow for ^{40}Ca with spherical *BUU*.
The degree of compression in the central cell ρ_c/ρ_0 (upper row), the average radial velocity v (middle row), and the root-mean-square radius R (lower row) as functions of time, for ^{40}Ca, calculated by imposing spherical symmetry in the *BUU* code. The results corresponding to different initial values of the compression parameter λ and the temperature T are indicated by the solid and dashed curves, respectively.

Figure 3: Collective flow for ^{197}Au with spherical *BUU*.
In a display similar to fig. 2 is shown ρ_c/ρ_0, v, and R for ^{197}Au.

Figure 4: Density profile for ^{40}Ca with spherical *BUU*.
Time evolution of the nuclear density profile for ^{40}Ca. The three sets of figures display results obtained from different compressed (solid curves) and thermal (dashed curves) initializations, corresponding to pairs of values of the temperature T and compression parameter λ that yield the same excitation energy (see fig. 1). The results have been obtained by imposing spherical symmetry in the *BUU* code.

Figure 5: Density profile for ^{197}Au with spherical *BUU*.
Time evolution of the nuclear density profile for ^{197}Au; similar to fig. 4.

Figure 6: Effect of the Coulomb field
The degree of compression in the central cell ρ_c/ρ_0 (upper left), the average radial velocity v (upper right), the root-mean-square radius R (lower left) as functions of time, and the density profile at 105 fm/c (lower right), for ^{197}Au compressed to $\lambda = 2.5$. The dashed lines indicate the results calculated without the Coulomb force, while the solid lines denote the results obtained by employing the full mean field (6).

Figure 7: Collective flow for ^{40}Ca with standard *BUU*.
The degree of compression in the central cell ρ_c/ρ_0 (upper row), the averaged radial velocity (middle row), and the root-mean-squar radius R (lower row) as functions of time, for ^{40}Ca initially compressed at $\lambda = 2.5$. The left and center columns correspond to standard *BUU* calculations with $\mathcal{N} = 200$ and 800, respectively. These curves are based on five independent simulation runs and the shaded area indicates the corresponding mean standard deviation. For reference the right column shows the *BUU* results obtained by imposing spherical symmetry.

Figure 8: Collective flow for ^{197}Au with standard *BUU*.
Results for ^{197}Au in a display similar to fig. 7.

Figure 9: Density distribution for ^{40}Ca with standard *BUU*.
Time evolution of the effective radial density profile $\bar{\rho}(r)$ for ^{40}Ca with $\lambda = 2.5$. The solid lines denote the calculation obtained by imposing spherical symmetry, while the dashed lines represent the average profile based on five independent standard *BUU* simulation runs, with $\mathcal{N}$=800 pseudo-particles per nucleon. The error bars indicate the corresponding standard deviation.

Figure 10: Density distribution for ^{40}Au with standard *BUU*.
Results for ^{197}Au, in a display similar to fig. 9 (also based on five independent runs), using $\lambda = 2$ and $\mathcal{N} = 300$.

Figure 11: Angular pattern.
Time evolution of the density distribution projected onto the unit sphere, $\tilde{\rho}(\hat{\boldsymbol{r}}, t)$, as a function of the polar angle θ and the azimuthal angle ϕ, for ^{197}Au initially compressed to double density $\lambda = 2$. The dashed contour lines correspond to the unity (corresponding to a spherically symmetric distribution), while the solid contours lines limit delineate the areas having values 2, 3, 4 and so on. The results were obtained with a standard *BUU* simulation using $\mathcal{N}$=300.

Figure 12: Pattern coefficients.
The time evolution of the pattern coefficients a_l, defined in eq. (15), for an ensemble of five different *BUU* histories, (each using $\mathcal{N}$=300), starting from ^{197}Au compressed to double density ($\lambda = 2$). The curves are drawn through the ensemble-averaged values, while the error bars indicate the associated dispersions.

Figure 13: $\mathcal{N}$ dependence of the angular pattern.
The density distribution projected onto the unit sphere, $\tilde{\rho}(\hat{\boldsymbol{r}}, t)$, at different stages of the evolution, for ^{197}Au initially compressed to double density ($\lambda = 2$), as obtained from one typical standard *BUU* simulation using either $\mathcal{N} = 100$ (left) or $\mathcal{N} = 300$ (right). The display is as in fig. 11.

Figure 14: $\mathcal{N}$ dependence of the pattern coefficients.
The time evolution of the pattern coefficients a_l for individual events obtained by using $\mathcal{N} = 100$ (upper figure) and $\mathcal{N} = 300$ (lower figure), for the same *BUU* histories shown in fig. 13.

Figure 15: $\mathcal{N}$ dependence of the radial flow and density profile.
Time evolution of the radial velocity v for the region that corresponds to $r < 20$ fm, obtained by a simulation with $\mathcal{N} = 100$ (dashed line) and $\mathcal{N} = 300$ (solid line), for the single *BUU* histories displayed in fig. 13. The corresponding effective density profiles $\bar{\rho}(r)$ are displayed in the upper-right corner at selected times.

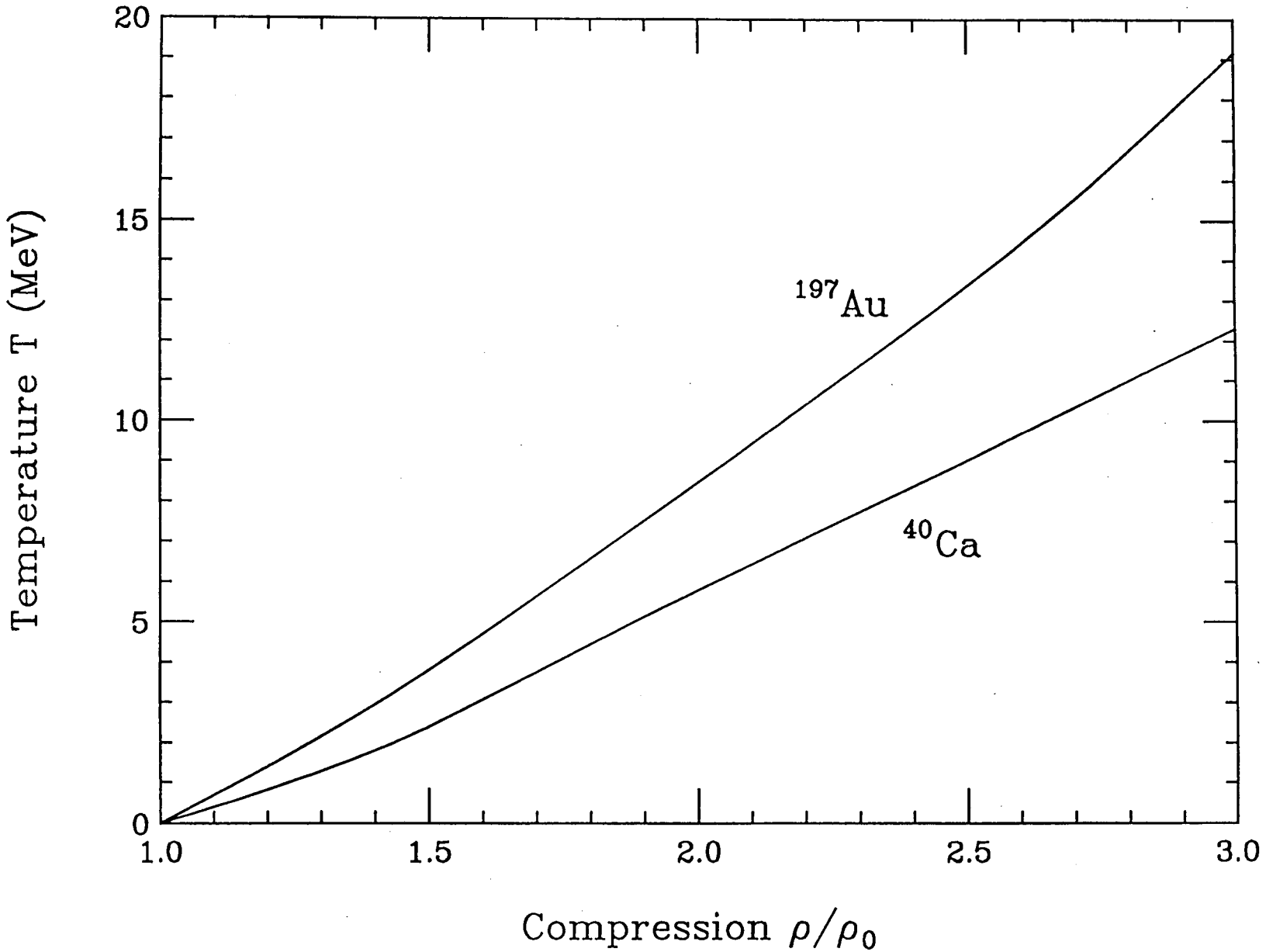
20
15
10
5
0
1.0
1.5
2.0
2.5
3.0
Temperature T (MeV)
Compression ρ/ρ_0
^{197}Au
^{40}Ca

Figure 1

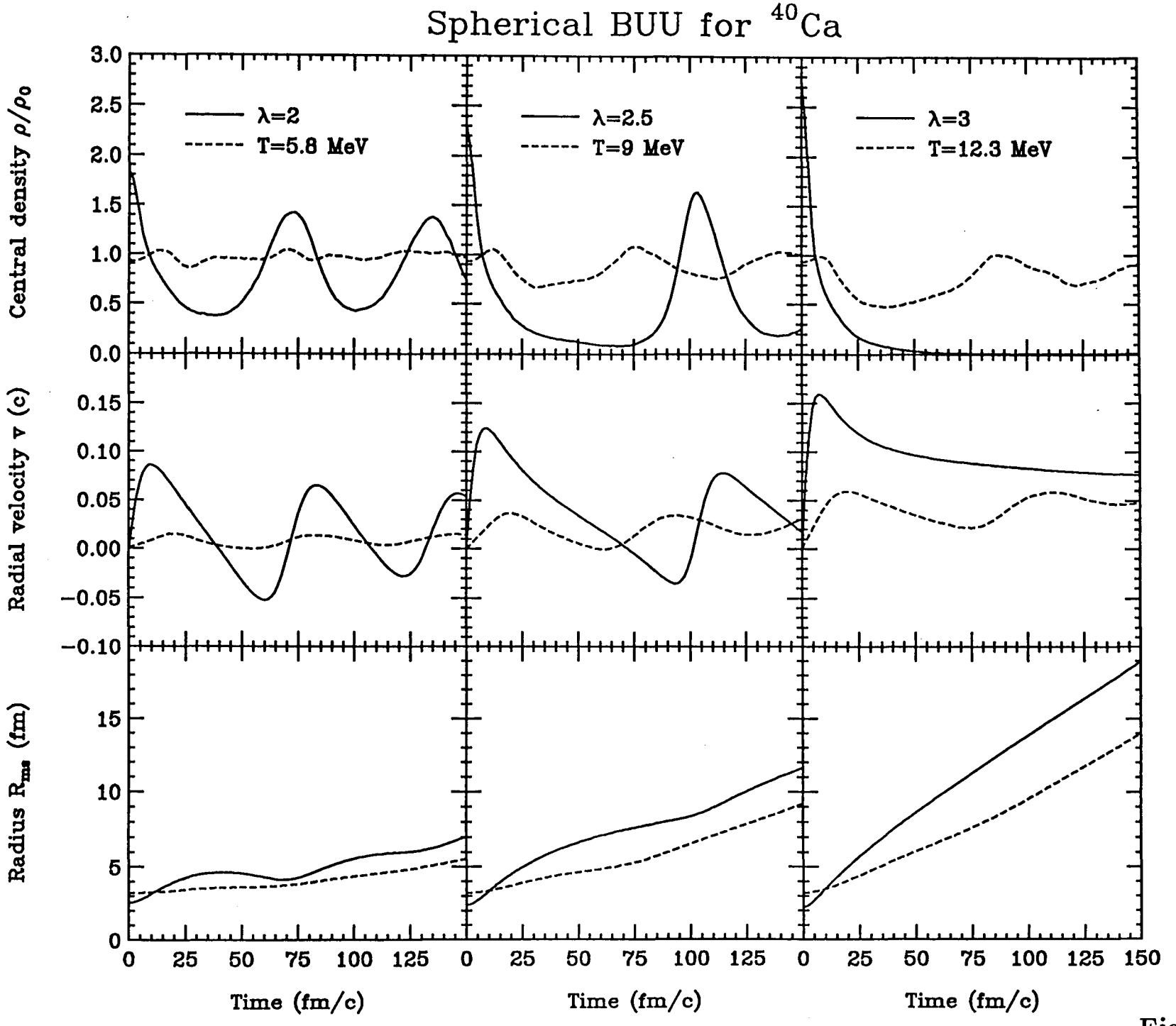
Spherical BUU for ^{40}Ca
λ=2
T=5.8 MeV
λ=2.5
T=9 MeV
λ=3
T=12.3 MeV
Central density ρ/ρ₀
Radial velocity v (c)
Radius R_ms (fm)
Time (fm/c)
Time (fm/c)
Time (fm/c)

Figure 2

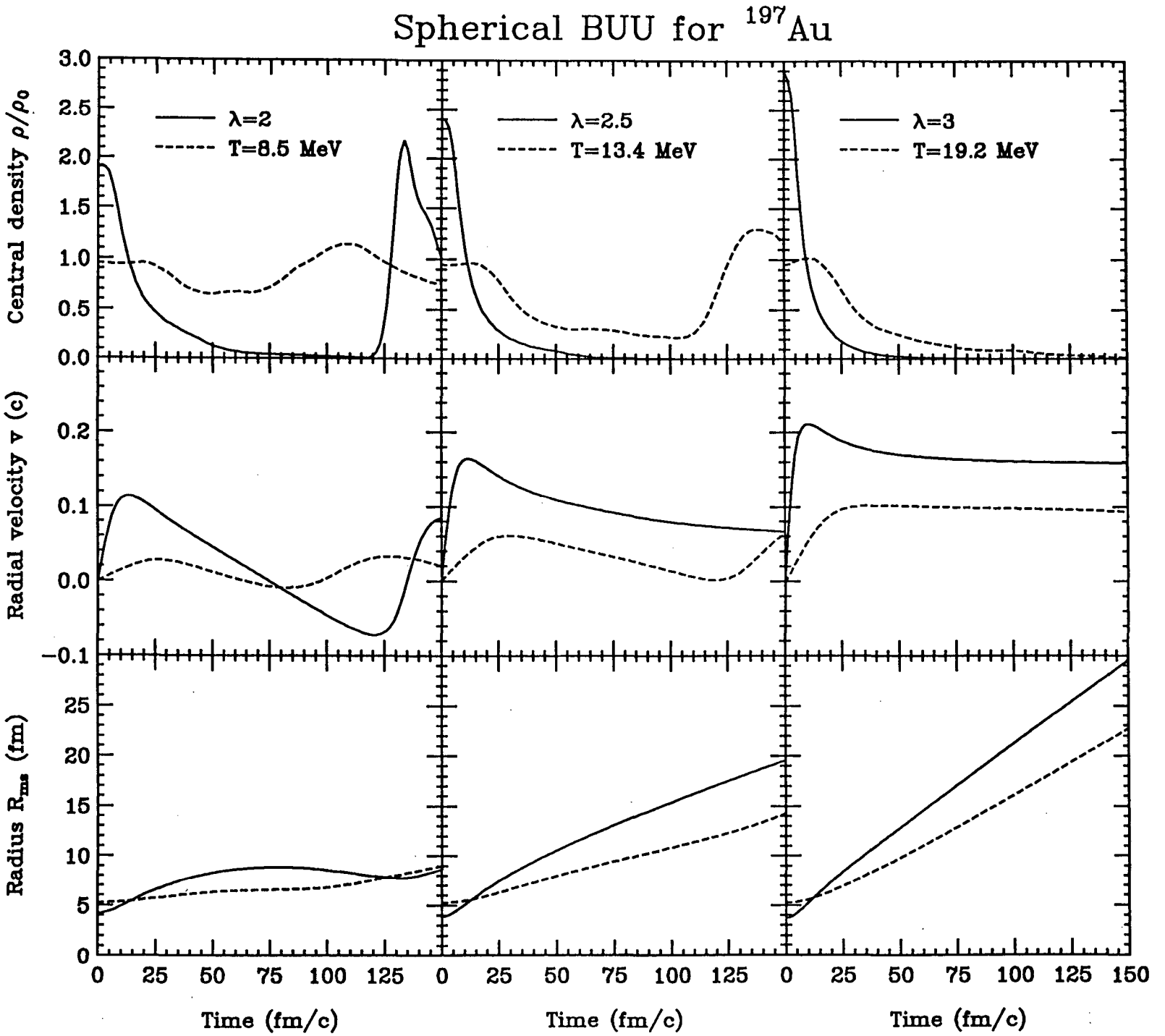
Spherical BUU for ^{197}Au
Central density ρ/ρ_0
Radial velocity v (c)
Radius R_{ms} (fm)
λ=2
T=8.5 MeV
λ=2.5
T=13.4 MeV
λ=3
T=19.2 MeV
Time (fm/c)
Time (fm/c)
Time (fm/c)

Figure 3

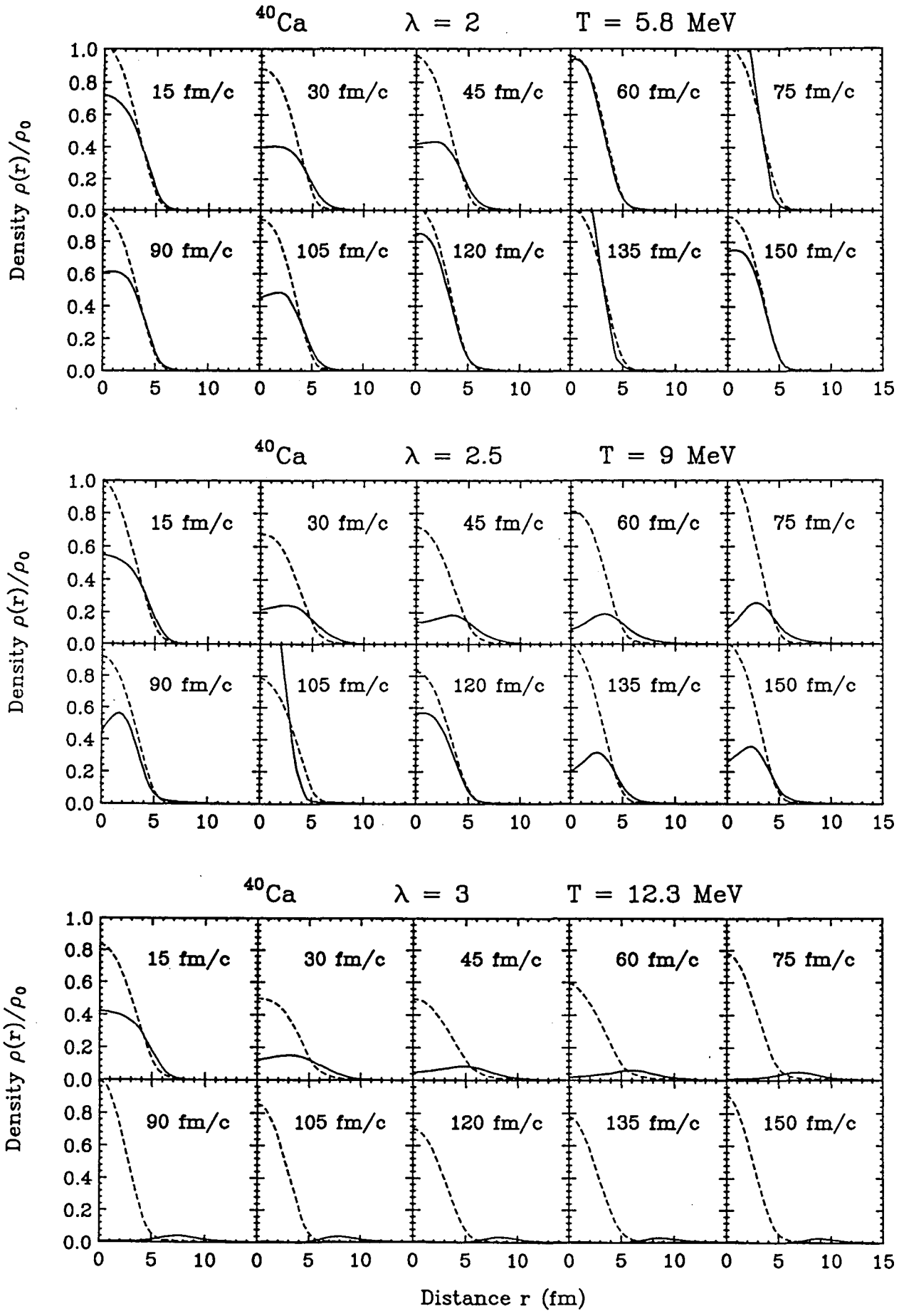
^{40}Ca λ = 2 T = 5.8 MeV
^{40}Ca λ = 2.5 T = 9 MeV
^{40}Ca λ = 3 T = 12.3 MeV
15 fm/c
30 fm/c
45 fm/c
60 fm/c
75 fm/c
90 fm/c
105 fm/c
120 fm/c
135 fm/c
150 fm/c
Density ρ(r)/ρ₀
Distance r (fm)

Figure 4

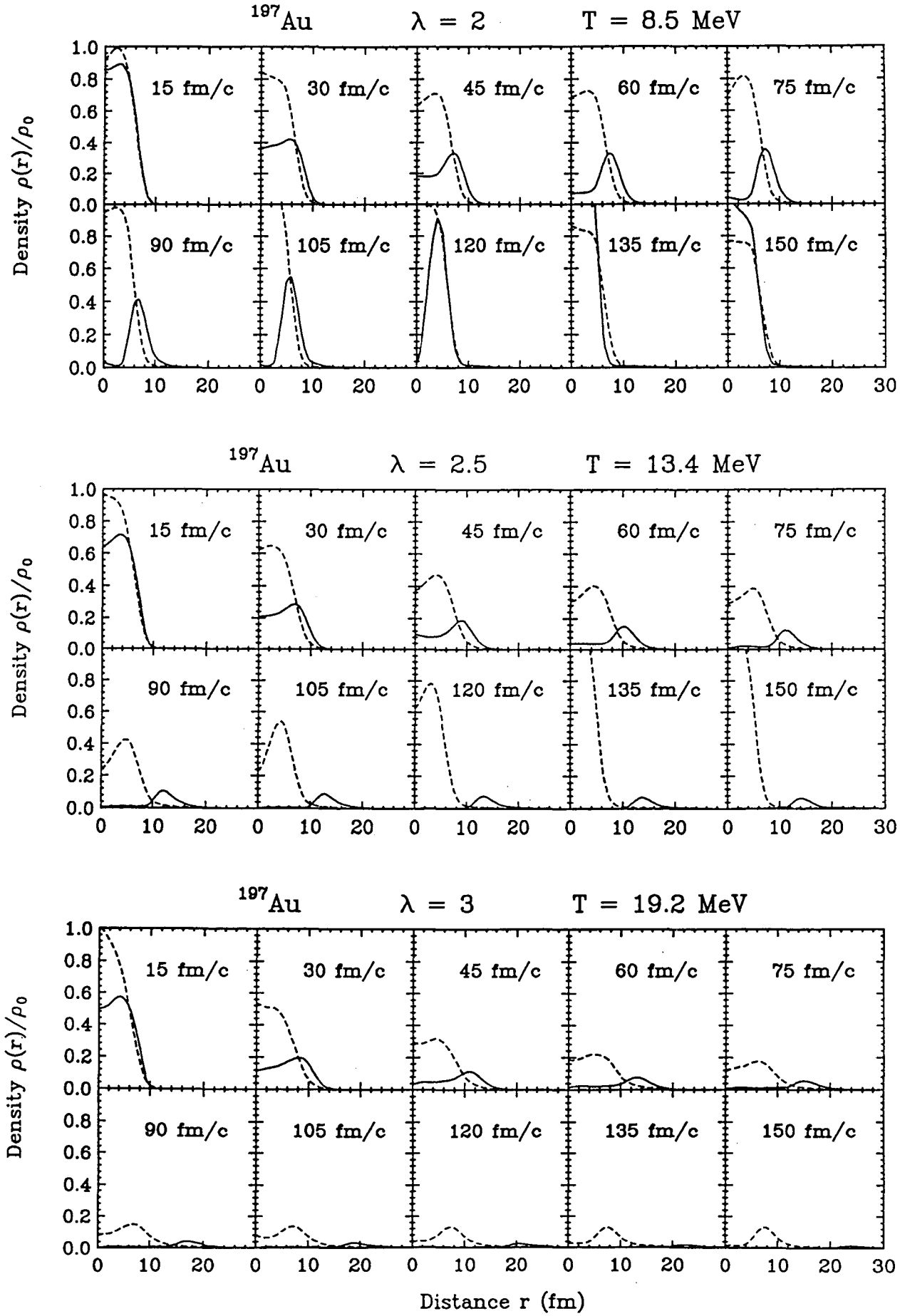
^{197}Au λ = 2 T = 8.5 MeV
^{197}Au λ = 2.5 T = 13.4 MeV
^{197}Au λ = 3 T = 19.2 MeV
15 fm/c
30 fm/c
45 fm/c
60 fm/c
75 fm/c
90 fm/c
105 fm/c
120 fm/c
135 fm/c
150 fm/c
Density ρ(r)/ρ₀
Distance r (fm)

Figure 5

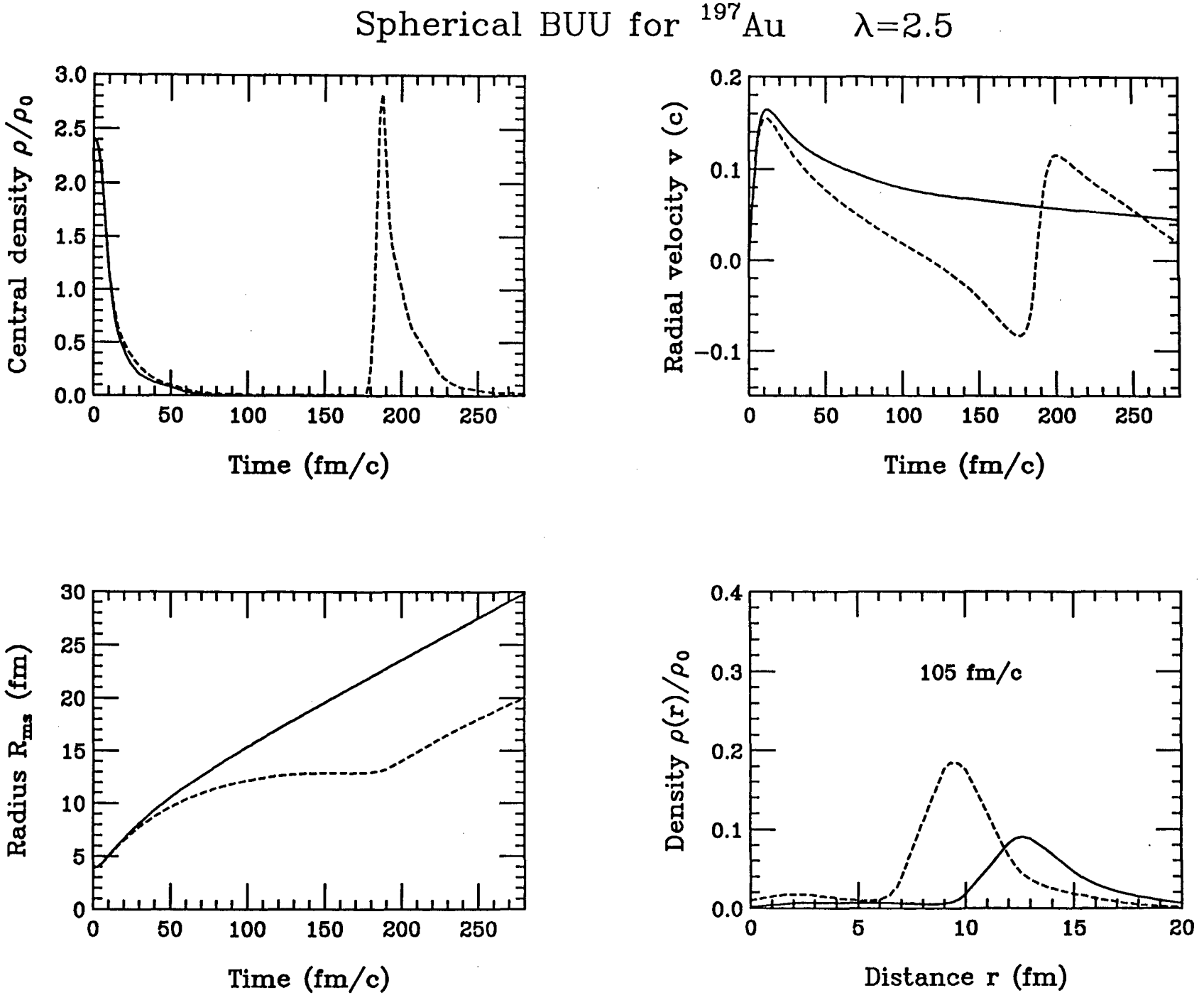
Spherical BUU for ^{197}Au λ=2.5
Central density ρ/ρ_0
Time (fm/c)
Radial velocity v (c)
Time (fm/c)
Radius R_{ms} (fm)
Time (fm/c)
105 fm/c
Density $\rho(r)/\rho_0$
Distance r (fm)

Figure 6

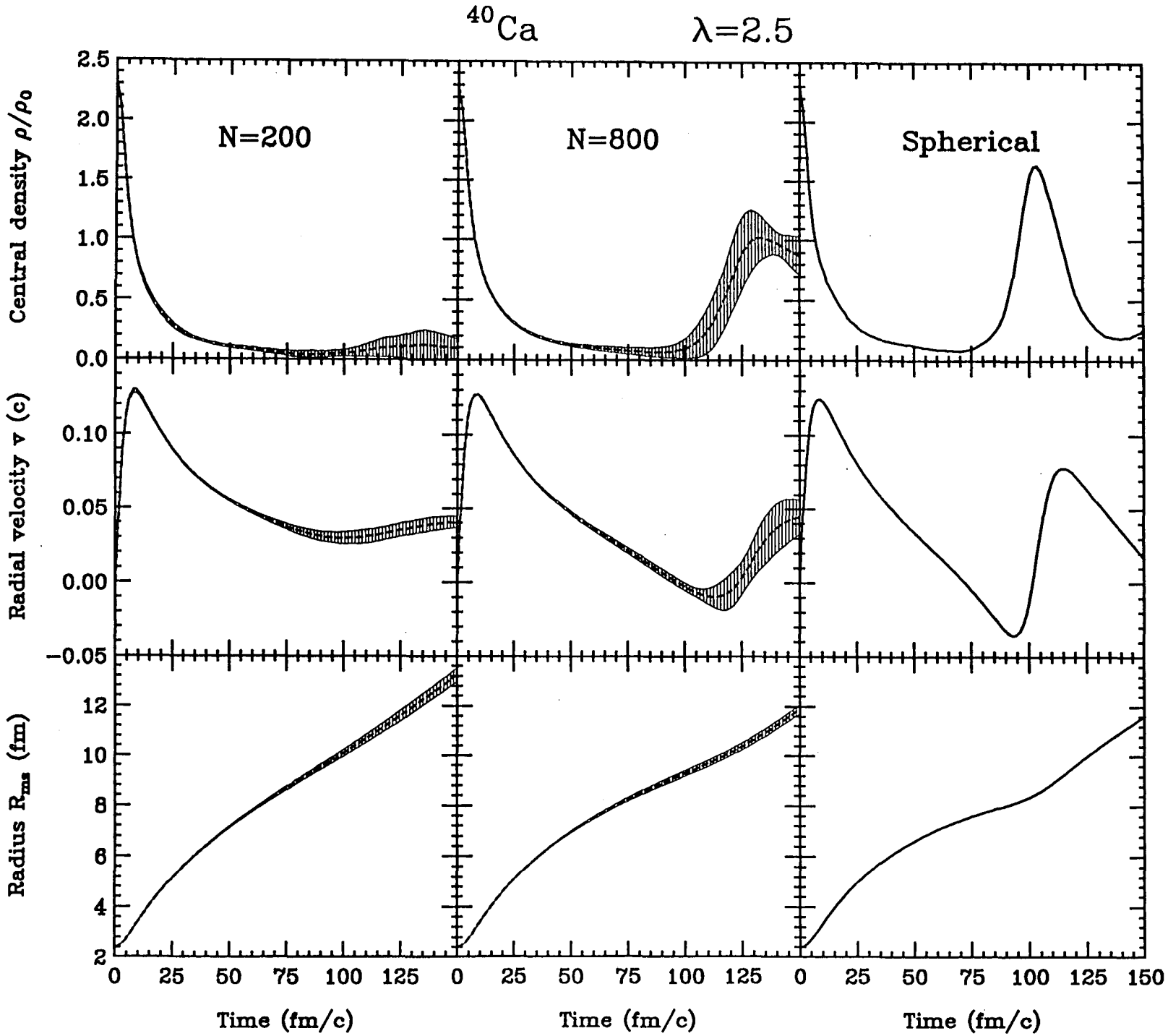
^{40}Ca
λ=2.5
N=200
N=800
Spherical
Central density ρ/ρ₀
Radial velocity v (c)
Radius R_ms (fm)
Time (fm/c)
Time (fm/c)
Time (fm/c)

Figure 7

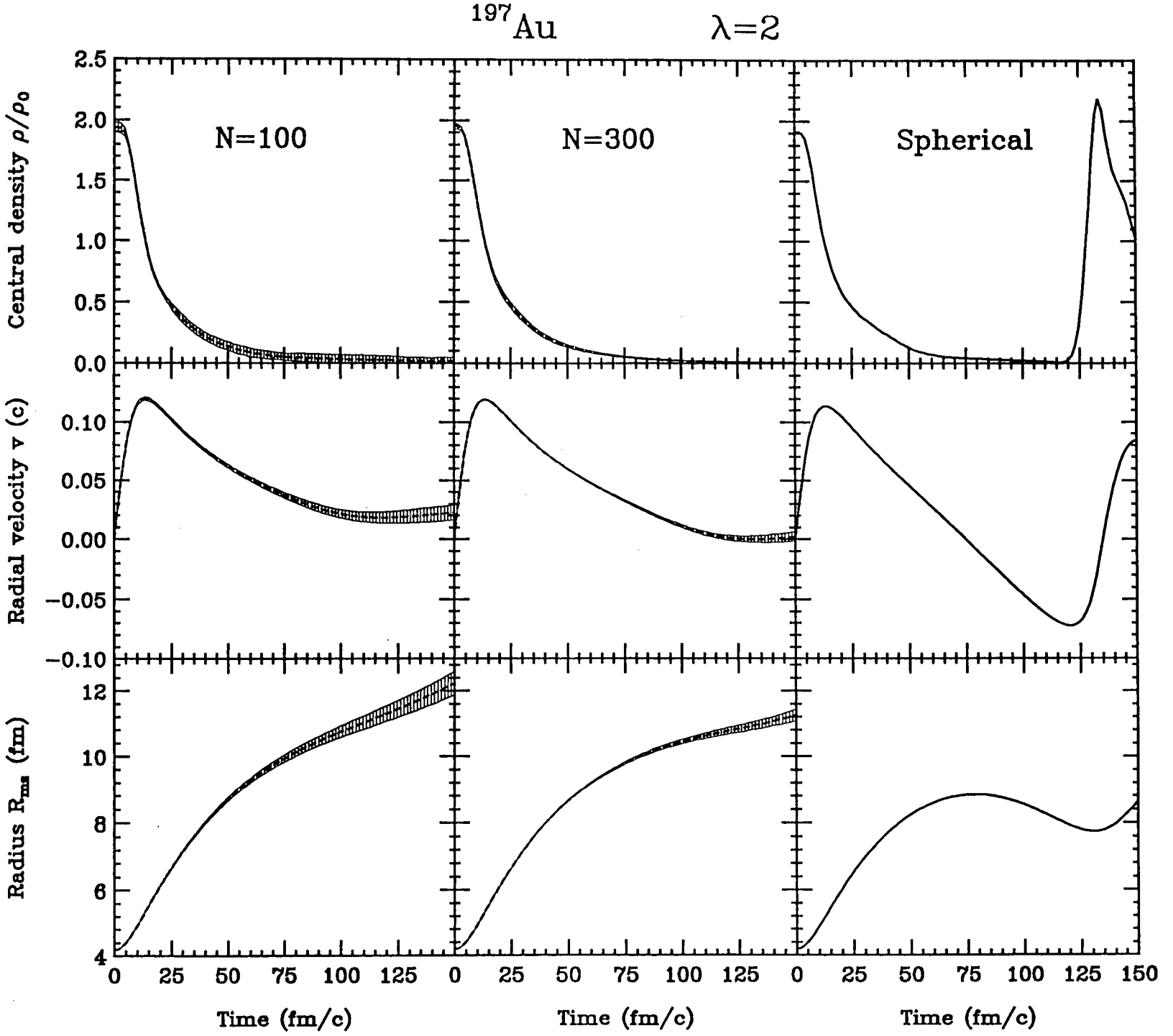
^{197}Au λ=2
N=100
N=300
Spherical
Central density ρ/ρ₀
Radial velocity v (c)
Radius R_ms (fm)
Time (fm/c)
Time (fm/c)
Time (fm/c)

Figure 8

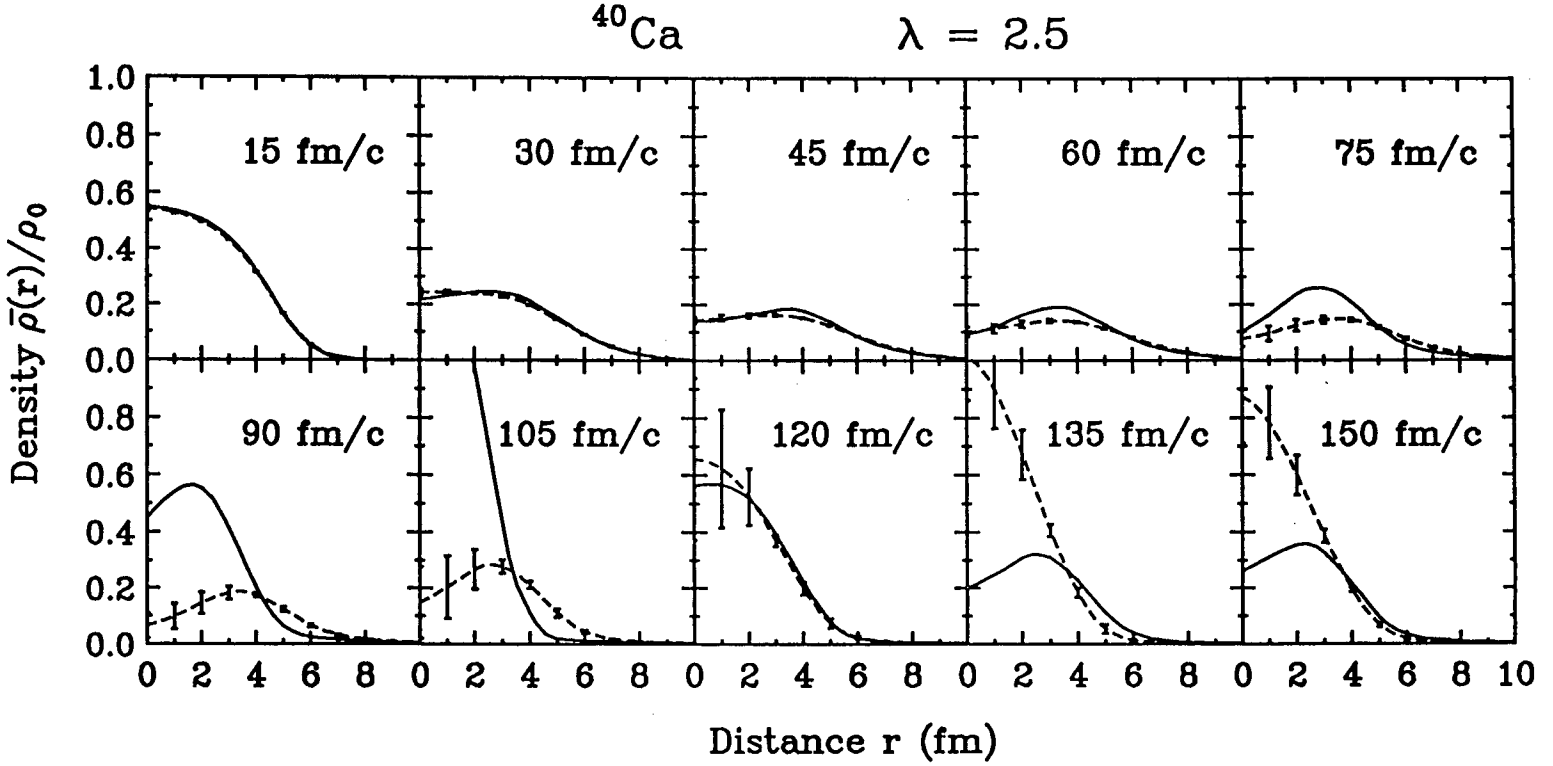
^{40}Ca
λ = 2.5
15 fm/c
30 fm/c
45 fm/c
60 fm/c
75 fm/c
90 fm/c
105 fm/c
120 fm/c
135 fm/c
150 fm/c
Density $\bar{\rho}(r)/\rho_0$
Distance r (fm)

Figure 9

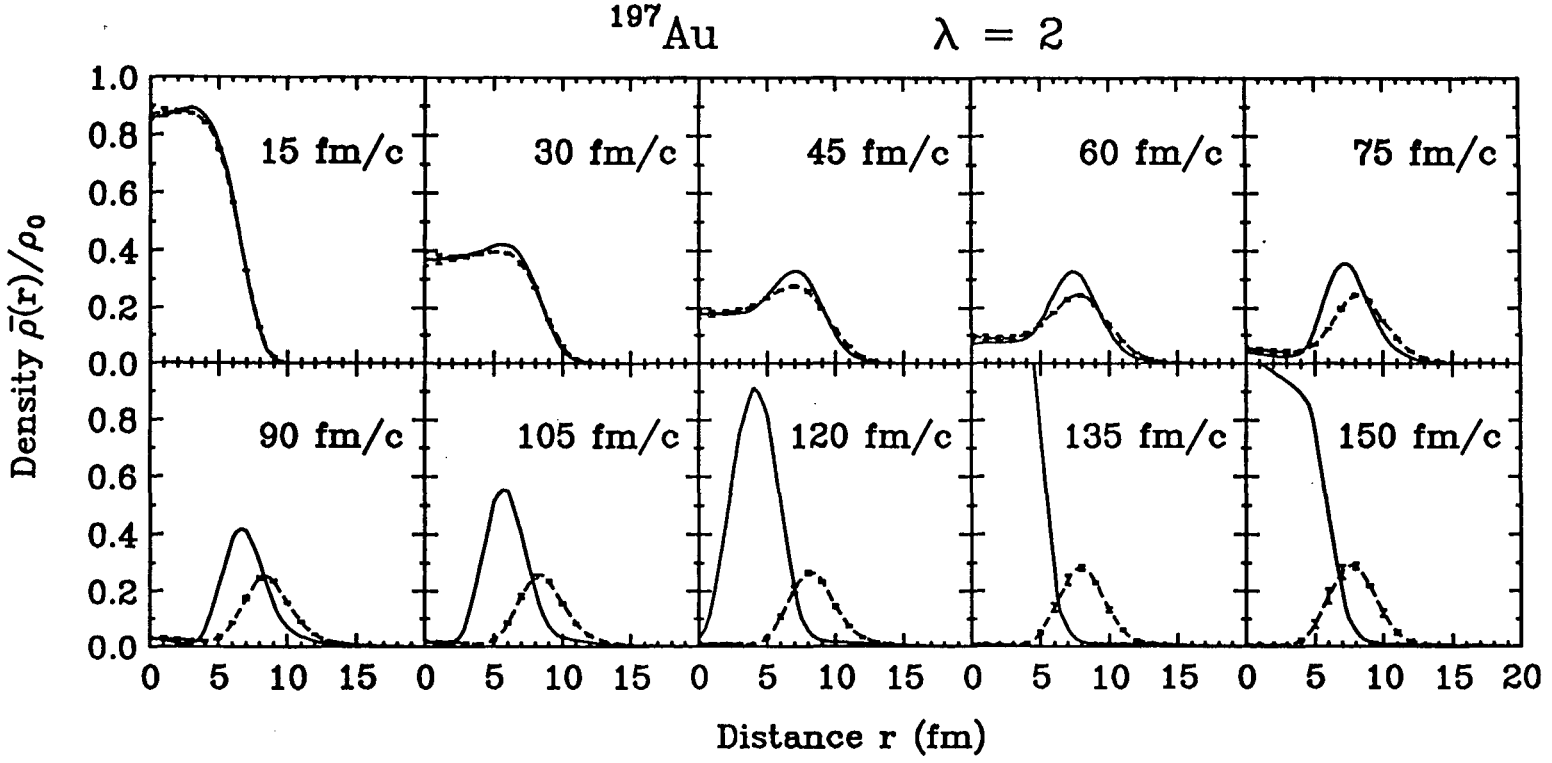
^{197}Au
λ = 2
15 fm/c
30 fm/c
45 fm/c
60 fm/c
75 fm/c
90 fm/c
105 fm/c
120 fm/c
135 fm/c
150 fm/c
Density $\bar{\rho}(r)/\rho_0$
Distance r (fm)
1.0
0.8
0.6
0.4
0.2
0.0
0
5
10
15
20

Figure 10

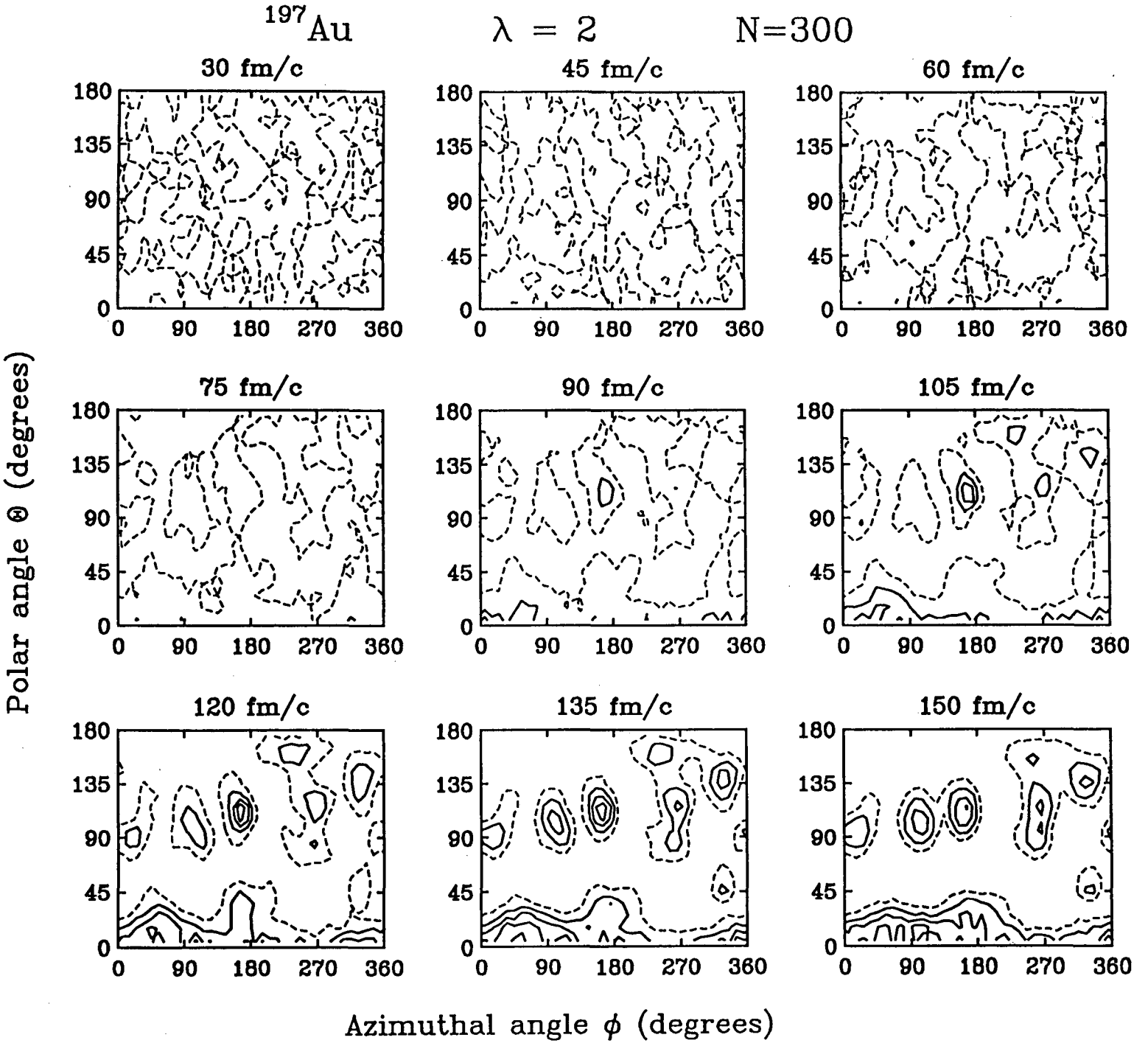
^{197}Au λ = 2 N=300
30 fm/c
45 fm/c
60 fm/c
75 fm/c
90 fm/c
105 fm/c
120 fm/c
135 fm/c
150 fm/c
0 45 90 135 180
0 90 180 270 360
Polar angle Θ (degrees)
Azimuthal angle φ (degrees)

Figure 11

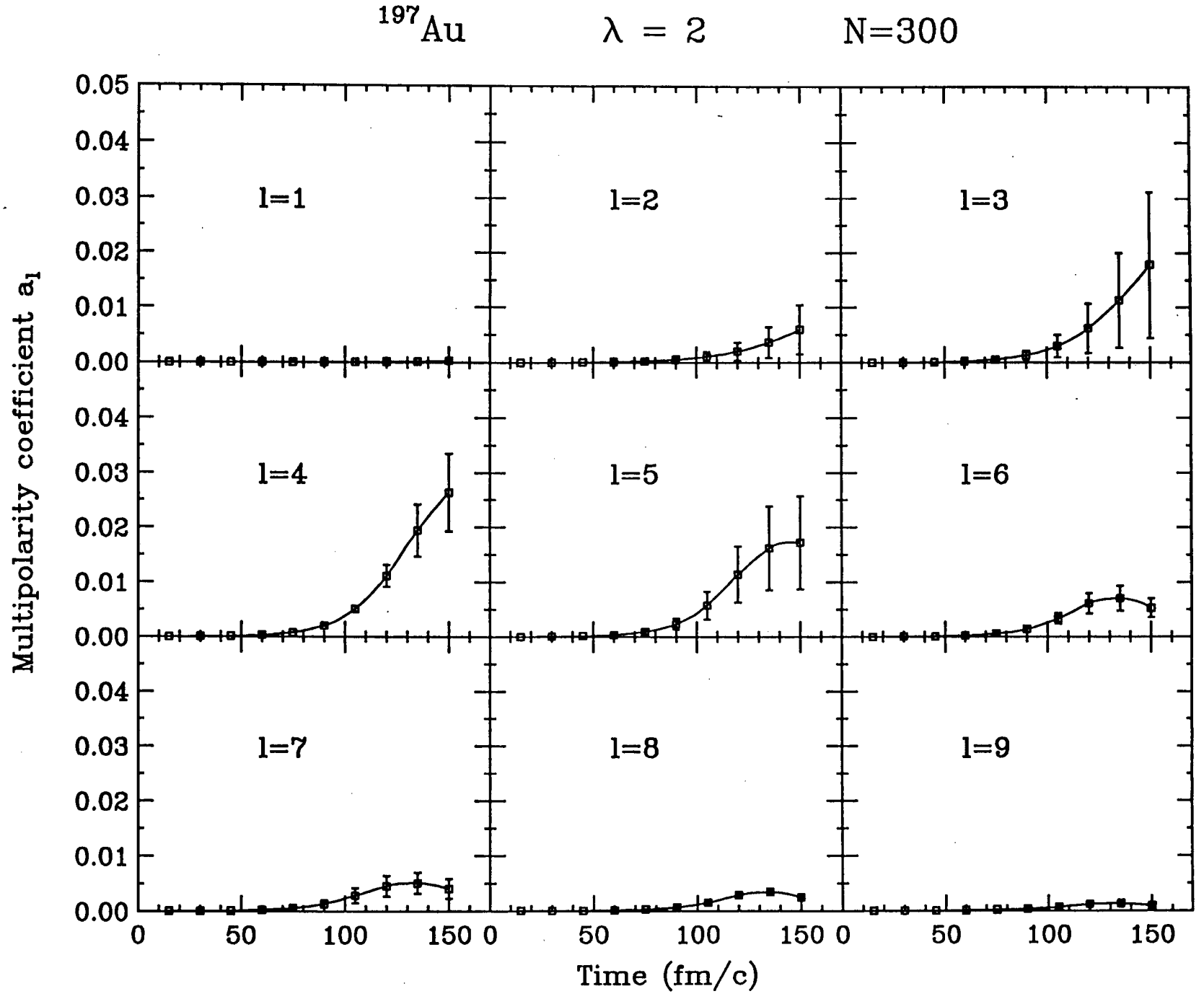
^{197}Au λ = 2 N=300
Multipolarity coefficient a_l
Time (fm/c)
l=1
l=2
l=3
l=4
l=5
l=6
l=7
l=8
l=9
0.05
0.04
0.03
0.02
0.01
0.00
0
50
100
150

Figure 12

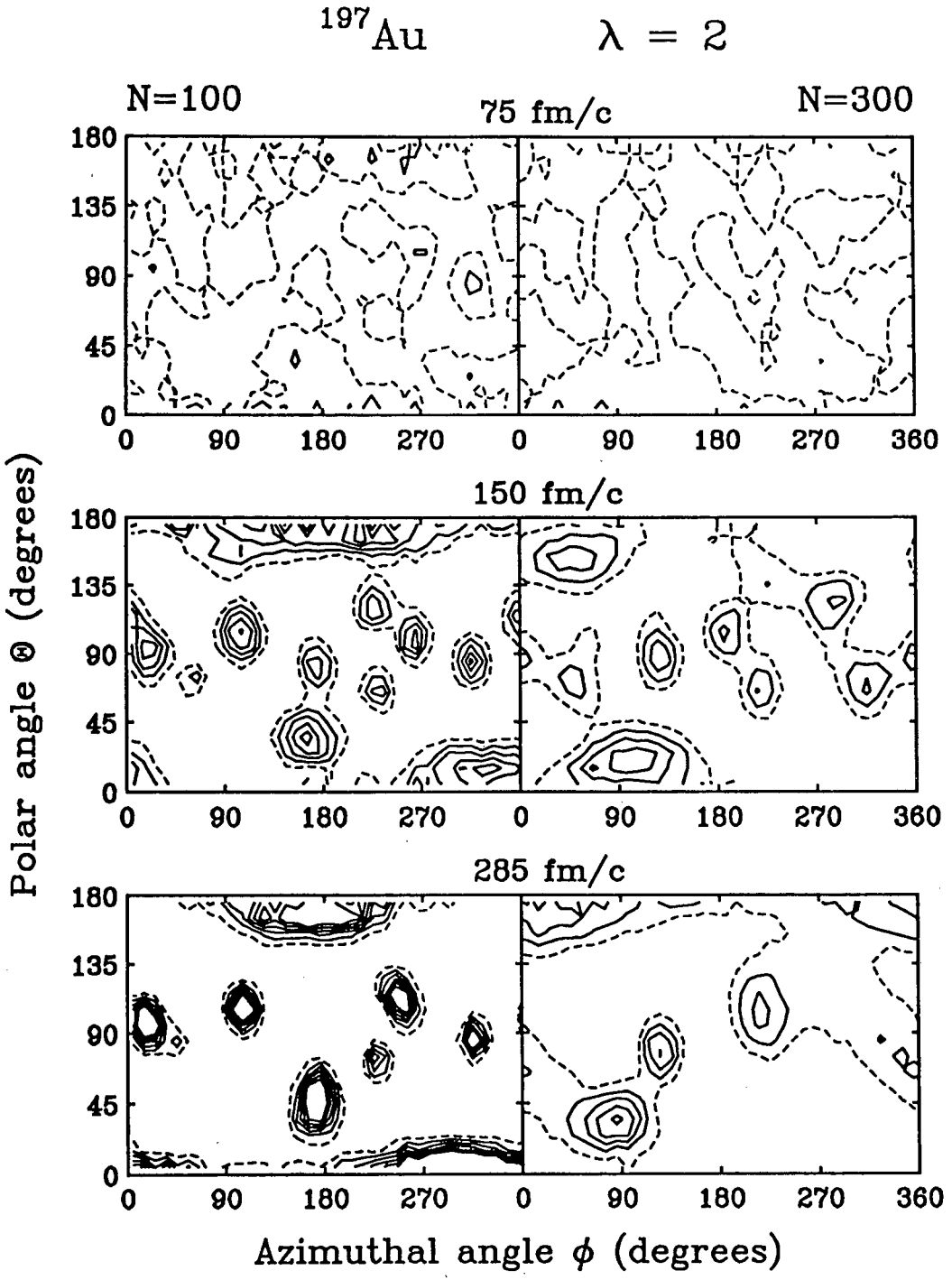
^{197}Au λ = 2
N=100
75 fm/c
N=300
150 fm/c
285 fm/c
Polar angle Θ (degrees)
Azimuthal angle φ (degrees)
0
45
90
135
180
0
90
180
270
360

Figure 13

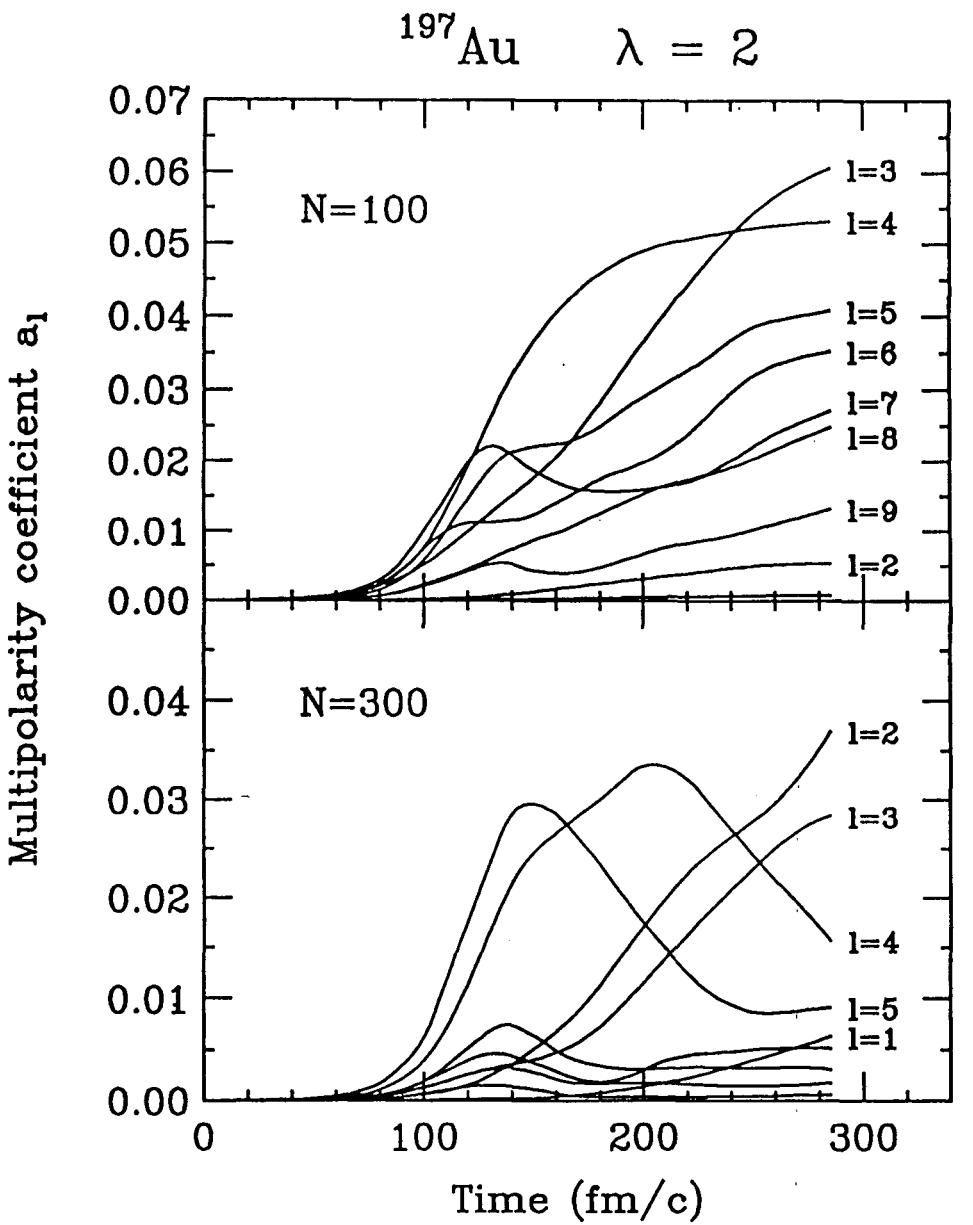
^{197}Au λ = 2
N=100
N=300
l=3
l=4
l=5
l=6
l=7
l=8
l=9
l=2
l=2
l=3
l=4
l=5
l=1
Multipolarity coefficient a_l
Time (fm/c)
0.07
0.06
0.05
0.04
0.03
0.02
0.01
0.00
0
100
200
300

Figure 14

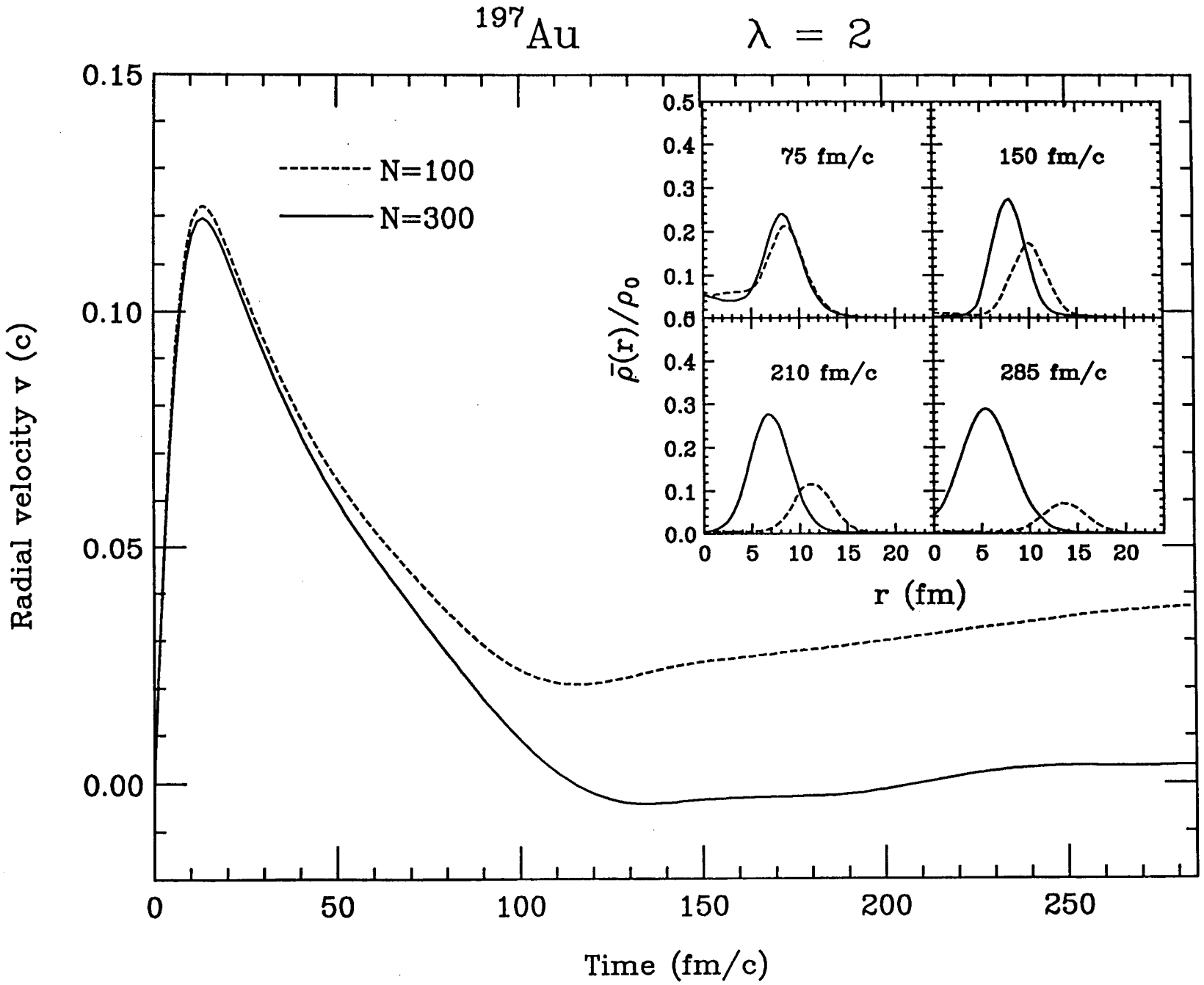
^{197}Au
λ = 2
N=100
N=300
Radial velocity v (c)
Time (fm/c)
0.15
0.10
0.05
0.00
0
50
100
150
200
250
75 fm/c
150 fm/c
210 fm/c
285 fm/c
$\bar{\rho}(r)/\rho_0$
r (fm)

Figure 15

LAWRENCE BERKELEY LABORATORY
UNIVERSITY OF CALIFORNIA
TECHNICAL INFORMATION DEPARTMENT
BERKELEY, CALIFORNIA 94720